

1
2
3
4
5
6
7
8
9
10
11
12
13
14
15
16

Medium-range predictability of early summer sea ice thickness distribution in the East Siberian Sea based on the TOPAZ4 ice-ocean data assimilation system

Takuya Nakanowatari^{1,*}, Jun Inoue¹, Kazutoshi Sato¹, Laurent Bertino², Jiping Xie², Mio Matsueda³, Akio Yamagami³, Takeshi Sugimura¹, Hironori Yabuki¹, and Natsuhiko Otsuka⁴

¹National Institute of Polar Research, 10-3, Midori-cho, Tachikawa-shi, Tokyo, 190-8518, Japan;

²Nansen Environmental and Remote Sensing Center, Thormøhlens gate 47, N-5006 Bergen,

Norway; ³Center for Computational Sciences, University of Tsukuba, 1-1-1 Tennodai, Tsukuba,

Ibaraki 305-8577, Japan; ⁴Arctic Research Center, Hokkaido University, Kita-21 Nishi-11 Kita-ku,

Sapporo, 001-0021, Japan

*Corresponding author: Takuya Nakanowatari, E-mail: nakanowatari.takuya@nipr.ac.jp

Abstract

Accelerated retreat of Arctic Ocean summertime sea ice has focused attention on the potential use of the Northern Sea Route (NSR), for which sea ice thickness (SIT) information is crucial for safe maritime navigation. This study evaluated the medium-range (lead time below 10 days) forecast skill of SIT distribution in the East Siberian Sea (ESS) in early summer (June–July) based on the TOPAZ4 ice ocean data assimilation system. Comparison of the operational model SIT data to reliable SIT estimates (hindcast, satellite, and in situ data) showed that the TOPAZ4 reanalysis reproduces qualitatively the tongue-like distribution of SIT in ESS in early summer and the seasonal variations. Pattern correlation analysis of the SIT forecast data over 3 years (2014–2016) reveals that the early summer SIT distribution is skillfully predicted for a lead time of up to 3 days, but that the prediction skill drops abruptly after the 4th day, which is related to dynamical process controlled by synoptic-scale atmospheric fluctuations. For longer lead times (>4 days), the thermodynamic melting process takes over, which makes most of the remaining prediction skill. In July 2014, during which an ice-blocking incident occurred, relatively thick SIT (~150 cm) was simulated over the ESS, which is consistent with the reduction of vessel speed. These results suggest that TOPAZ4 sea ice information has a great potential for practical applications in summertime maritime navigation via the NSR.

35 **1 Introduction**

36 During recent decades, sea ice cover in the Northern Hemisphere has shown remarkable
37 reduction and the largest rates of decrease of $100,000 \text{ km}^2 \text{ decade}^{-1}$ has been observed in the
38 western Arctic Ocean in summer [Cavalieri and Parkinson, 2008]. Sea ice retreat influences the
39 light conditions for phytoplankton photosynthesis activity [Wassmann, 2011], and the resultant
40 meltwater influences the marine environment via ocean acidification [Yamamoto-Kawai et al.,
41 2011]. In winter, shrinkage of the sea ice area in marginal seas, such as the Barents Sea changes the
42 surface boundary conditions of the atmosphere, influences planetary waves, and causes blocking
43 events that are one of the possible causes of the recent severe winters in mid-latitude regions
44 [Honda et al., 2009; Inoue et al., 2012; Mori et al., 2014; Overland et al., 2015; Petoukhov and
45 Semenov, 2010; Screen, 2017].

46 In contrast to these climatic consequences and problems for the marine ecosystem caused by
47 the reduction in sea ice, the retreat of Arctic sea ice has new opportunities for commercial maritime
48 navigation. It has been reported that exploitation of shipping routes in the Arctic Ocean, i.e., the
49 Northern Sea Route (NSR), could reduce the navigational distance between Europe and Asia by
50 about 40% in comparison with routes via the Suez Canal [Schøyen and Bråthen, 2011]. Melia et al.
51 [2016] discussed the possibility of a viable trans-Arctic shipping route in the 21st century, based on
52 the Coupled Model Intercomparison Project Phase 5 (CMIP5) global climate model simulation.
53 Currently, the summertime use of the NSR by commercial vessels such as cargo ships and tankers
54 has increased [Eguíluz et al., 2016]. Therefore, obtaining precise information on sea ice condition
55 and evaluating the forecast skill of operational sea ice models have become urgent issues.

56 Many previous studies have examined the predictability of summertime sea ice change in the
57 Arctic Ocean in terms of its coverage [Wang et al., 2013] and motion [Schweiger and Zhang, 2015].
58 Kimura et al. [2013] reported a good correlation of the spatial distribution of summertime sea ice
59 concentration (SIC) with winter ice divergence/convergence. Their study indicated that sea ice

60 thickness (SIT) or sea ice volume before the melt season is a source of predictability for
61 summertime SIC. Recently, their study was supported by hindcast experiments undertaken using a
62 climate model, in which the SIC in the East Siberian Sea (ESS) was shown to have significant
63 seasonal prediction skill [Bushuk et al., 2017]. The significant impacts of SIT condition on the
64 seasonal prediction of SIC in the Arctic Ocean have been highlighted by many studies [Lindsay et
65 al., 2008; Holland et al., 2011; Blanchard-Wrigglesworth and Bitz, 2014; Collow et al., 2015; Melia
66 et al., 2015; Chen et al. 2017; Melia et al. 2017]. Thus, the persistence of SIT or sea ice volume is
67 one of the key factors determining the skill of seasonal predictions of summertime sea ice area.

68 Earlier studies have focused primarily on the seasonal to interannual predictability of SIC or
69 sea ice area in the Arctic Ocean; thus, subseasonal variation in SIT and its predictability have not
70 been examined fully for near-term route planning. Although the summertime sea ice extent has
71 rapidly decreased on interannual timescale, substantial sea ice area still remains in critical stretches
72 of the NSR such as the ESS in early summer (June–July). Since precise information regarding SIT
73 and its near-future condition is crucial for icebreaker operations [Tan et al., 2013; Pastusiak, 2016],
74 it is important to clarify the medium-range (3 to 10 days lead time) predictability of summertime
75 SIT in the Arctic Ocean.

76 Synoptic-scale fluctuations of cyclone and anticyclone is greater over the Arctic Ocean and
77 Eurasia in summer than in winter [Serreze and Barry, 1988; Serreze and Barrett, 2008]. In recent
78 years, there is a risk that an Arctic cyclone becomes extremely developed and covered the entire
79 Pacific sector [Simmonds and Rudeva, 2012; Yamagami et al. 2017]. Because the ESS corresponds
80 to the route of Arctic cyclones generated over the Eurasian Continent [Orsolini and Sorteberg,
81 2009], it is expected that synoptic-scale atmospheric fluctuations would influence substantially the
82 spatial distribution of SIT and ice motion in the ESS. Ono et al. [2016] highlighted the importance
83 of atmospheric prediction skill on medium-range forecasts of sea ice distribution in the ESS based
84 on a case of an extreme cyclone that occurred on 6 August 2012. On the other hand, earlier studies

85 pointed out that the sea ice melting process is important for the long-term prediction of summertime
86 sea ice extent [e.g., Bushuk et al., 2017]. But the relative importance of dynamical and
87 thermodynamic processes on the medium-range forecast skill of summertime sea ice properties has
88 not yet been well understood.

89 Since 2010, ice–ocean forecasts and a 20-years reanalysis are available for the Arctic Ocean,
90 based on the TOPAZ ocean data assimilation system (Towards an Operational Prediction system for
91 the North Atlantic European coastal Zones) in its 4th version [Sakov et al., 2012]. The Norwegian
92 Meteorological Institute provides 10-day forecast products in daily mean fields, forced at the
93 surface by the European Centre for Medium-Range Weather Forecasts (ECMWF) operational
94 atmospheric forecasts, updated daily and distributed by the Copernicus Marine Environment
95 Monitoring Services (<http://marine.copernicus.eu>). The reliability of the corresponding TOPAZ4
96 reanalysis data has been evaluated previously through comparison with in situ and satellite SIT data
97 [Xie et al. 2017]. They showed the SIT in the TOPAZ4 reanalysis data are comparable to observed
98 values over the Beaufort Gyre and central Arctic Ocean, although the SIT overall shows a negative
99 bias of several dozen centimeters throughout a year. Thus, it is expected that the SIT data in the
100 TOPAZ reanalysis data should also be reliable in the ESS even in the melting season, and the
101 forecast SIT data should show skillful prediction skill on medium-range time scale.

102 In this study, we examined the predictability of the early summer SIT distribution in the ESS
103 on the medium-range timescale and discussed its underlying physical mechanisms, based on the
104 TOPAZ4 forecast dataset and trivial dynamical and thermodynamical models. Section 2 describes
105 the data and methods. Section 3 evaluates the reliability of the SIT data in the TOPAZ4 reanalysis
106 data through comparison with all available in situ and satellite observations, as well as operational
107 model analyses, with particular emphasis on the ESS. In section 4, we examine the predictability of
108 the SIT distribution in the ESS based on TOPAZ4 forecast data. Section 5 examines the relationship
109 between sea ice conditions and vessel speed during an ice-blocking event that occurred in July 2014.

110 A discussion and the derived conclusions are presented in section 6.

111

112 **2 Data and Methods**

113 This study used daily mean sea ice data derived from the TOPAZ4 Arctic sea ice forecast
114 system dataset, in which the SSM/I SIC data, hydrographic temperature and salinity data,
115 along-track sea level anomaly, and satellite estimates of ice drift and sea surface temperature were
116 assimilated, but sea ice thickness was not yet assimilated in this version of the reanalysis [Simonsen
117 et al. 2017]. The TOPAZ4 system was designed as a regional ice–ocean coupled system forced with
118 atmospheric flux data. The ocean model of TOPAZ4 is based on version 2.2 of HYCOM, which
119 uses isopycnal vertical coordinates in the ocean interior and z level coordinates in the near-surface
120 layer. The sea ice model uses an elastic–viscous–plastic rheology [Hunke and Dukowicz, 1997].
121 The thermodynamic processes are based on a three-layer thermodynamic model with one snow and
122 2 ice layers [Semtner, 1976] with a modification for subgrid-scale ice thickness heterogeneities
123 [Fichefet and Morales Maqueda, 1997]. The model domain covers the Arctic Ocean and the North
124 Atlantic, and the lateral boundaries are relaxed to monthly mean climatological data. The spatial
125 resolution is 12–16 km with 28 hybrid layers, which constitutes eddy-permitting resolution in low-
126 and mid-latitude regions but not in the Arctic Ocean. In this system, in situ hydrographic
127 observations are assimilated together with satellite observations of the ocean such as sea surface
128 temperature and sea level anomaly. Since this system assimilates the SIC and sea ice velocity (but
129 the latter only in cold season), one should expect adequate simulation of SIT through the ridging
130 process [Stark et al. 2008]. It has been reported that the SIT of the TOPAZ4 reanalysis data has
131 substantial negative bias from 2001 to 2010 due to excessive snowfall, which has been modified
132 after 2011 [Xie et al., 2017]. Therefore, this study used SIT data from 1 January 2011 to 31
133 December 2014.

134 The data assimilation method of TOPAZ4 is a deterministic version of the ensemble Kalman

135 filter (EnKF) [Sakov and Oke, 2008] with an ensemble of 100 dynamical members. Since EnKFs
 136 have time-dependent state error covariances, this method is suitable for data assimilation of
 137 anisotropic variables in areas close to the sea ice edge [Lisæter et al. 2003, Sakov et al. 2012]. The
 138 TOPAZ4 reanalysis data were produced with the 6-hourly forcing from the ERA Interim reanalysis
 139 [Dee et al., 2011]. The surface turbulent heat flux and momentum flux were both calculated using
 140 bulk formula parameterizations [Kara et al., 2000; Large and Pond, 1981]; thus, instead of the
 141 ERA-Interim fluxes themselves. The forecast and reanalysis systems have almost the same settings
 142 and their results are similar during their overlap period (not shown).

143 To evaluate the prediction skill of the TOPAZ4 forecast system, we used daily mean sea ice
 144 forecast data during 3 recent years from 2014 to 2016 [Simonsen et al. 2017]. A probabilistic
 145 10-member ensemble forecast was performed with the ECMWF medium-range (up to 10 days)
 146 atmospheric forecast data updated daily, out of which only the ensemble average is used. To
 147 produce 10 ensemble members in the TOPAZ4 forecast system, the ECMWF global atmospheric
 148 forecast data as well as several parameters of sea ice model are perturbed by adding stochastic
 149 forcing term [Evensen, 2003]. In this study, we excluded the forecast data in July 2014, because of
 150 a real-time forecast production incident (the forecast were in free-running mode then) [H. Engedahl,
 151 personal communication]. Since the forecast data were only provided weekly before 2016, the total
 152 of 150 cases was assembled during the study period. The skill core was quantified using pattern
 153 correlation coefficients (PCCs), which are used widely in deterministic forecast verification
 154 [Barnett and Schlesinger, 1987]:

$$155 \quad PCC = \frac{\sum_{ij=1}^N (f_{ij} - \bar{f}_{ij})(a_{ij} - \bar{a}_{ij})}{\sqrt{\sum_{ij=1}^N (f_{ij} - \bar{f}_{ij})^2} \sqrt{\sum_{ij=1}^N (a_{ij} - \bar{a}_{ij})^2}} \quad (1)$$

156 where f_{ij} and a_{ij} are forecast and analysis sea ice variables, respectively. The overbar denotes the
 157 average values over the analyzed area (see Fig. 1a); thus the PCC reflects the correlation of

158 observed and signal anomalies relative to their respective spatial means.

159 To evaluate the reliability of the SIT values in the TOPAZ4 reanalysis data in early summer,
160 we mainly used the Pan-Arctic Ice Ocean Modeling and Assimilation System (PIOMAS) outputs,
161 which are derived from the coupled ice–ocean modeling and assimilation system based on the
162 Parallel Ocean Program POP and the Thickness and Enthalpy Distribution (TED) sea ice model,
163 forced with NCEP-NCAR reanalysis data [Zhang et al., 2003]. In this dataset, SIC and sea surface
164 temperature are assimilated by adoptive nudging, and many studies [Schweiger et al., 2011; Lindsay
165 and Zhang, 2006; Stroeve et al., 2014] have compared PIOMAS output with observed SIT data and
166 found it the most reliable estimate of observed SIT in the Arctic Ocean [Laxon et al., 2013; Wang et
167 al. 2016].

168 As an alternative SIT data to evaluate the SIT distribution in the ESS, we used the merged
169 product of CryoSat-2 (CS2) and the Soil Moisture and Ocean Salinity (SMOS) SIT products
170 (hereafter, CS2SMOS) from 2011 to 2014 [Ricker et al. 2017], which were provided by the online
171 sea-ice data platform “meereisportal.de” (For details, acknowledgement) [Grosfeld et al. 2016].
172 These data are interpolated to 25-km resolution based on optimal interpolation and they are
173 available from October to April. In general, CS2 data have large uncertainty in the estimation of
174 SIT of <1 m, while the SMOS relative uncertainties are lowest for very thin ice. Thus, the merged
175 product is – to date – considered the best estimate of the satellite-based SIT distribution in and
176 around the ESS, although it was reported that there is potential negative bias in mixed first-year and
177 multiyear ice regions such as the Beaufort Sea [Ricker et al. 2017].

178 For the melting season (May–July), there is no reliable estimate of SIT distribution in the ESS,
179 we therefore used only in situ SIT data of autonomous ice mass balance (IMB) buoys obtained near
180 the ESS [Perovich et al., 2013]. During 2011 to 2014, total 4 buoys are available in a whole year
181 including the melting season (the period in each buoy is listed in Table 1). To compare the
182 two-dimensional SIT data with IMB buoy data, we re-gridded the gridded SIT data along the IMB

183 buoy trajectories. This comparison method is almost identical to that adopted by Sato and Inoue
184 [2017] who compared IMB buoy data with SIT data of the NCEP-CFSR reanalysis. Before
185 comparing the gridded SIT data with IMB buoy data in each grid point, we reconstructed these SIT
186 data on a 0.25° latitude–longitude grid by applying bilinear interpolation. The temporal and
187 horizontal resolutions of the observed and simulated SIT data are summarized in Table 1.

188 To examine the source of medium-range predictability in SIT distribution, we also used
189 ECMWF atmospheric forecast data on a 1.25° latitude–longitude grid from 2013 to 2016, derived
190 from the THORPEX Interactive Grand Global Ensemble through its data portal
191 (<http://tigge.ecmwf.int>). This dataset is very similar to the atmospheric forecast data used in the
192 TOPAZ4 operational forecast system [Simonsen et al. 2017]. For the examination of atmospheric
193 forecast skill, we used 51 ensemble daily means of zonal and meridional wind speed at 10-m height
194 on the same days as the TOPAZ4 forecast data at lead times of 0–10 day.

195 To evaluate the influence of sea ice condition on vessel speed in the ESS including the Laptev
196 and Kara Seas, we used the vessel speed data derived from Automatic Identification System (AIS)
197 from two tankers during their passage through the ESS on 4–26 July 2014, which were provided by
198 Shipfinder (<http://jp.shipfinder.com/>). The temporal resolution is about 2 to 3 hours, depending on
199 the timing and relative location of the satellite track and the ground-based receiver station of AIS
200 signal. Their ice classes correspond to IA Super in the Finnish–Swedish Ice Class Rules, and these
201 vessels are capable of navigating sea ice regions in which SIT is up to 50–90 cm. Both tankers were
202 likely to be hindered considerably by ice conditions, even under escort by Russian nuclear-powered
203 ice-breakers; thus, these AIS data are considered suitable for a case study of the influence of SIT on
204 icebreaker speed.

205

206 **3 Comparisons between TOPAZ4 and other available SIT data**

207 Figure 1a shows the spatial distribution of PIOMAS SIT in July in the Arctic marginal seas of

208 the Laptev Sea, ESS, and Chukchi Sea. The PIOMAS shows the tongue-like distribution of SIT,
209 characterized by relatively thick ice (>1.0 m) extending from the North Pole to the ESS. Since in
210 this region, sea ice motion tends to be converging during winter [Kimura et al. 2013], the sea ice is
211 likely to increase the thickness by ridging and rafting and thus remains until the next early summer.
212 These features are qualitatively simulated in the TOPAZ4 reanalysis data (Fig. 1b). The PCC of the
213 climatological SIT between TOPAZ4 and PIOMAS in the Arctic marginal seas (70° – 80° N,
214 120° E– 160° W, shown in Fig. 1a) is larger than 0.9 from March to July. The PCCs of the
215 climatological SIT between TOPAZ4 and CS2SMOS from March to April are 0.86 and 0.82, which
216 are comparable to those of PIOMAS (Table 2).

217 From the difference map of the climatological SIT between TOPAZ4 reanalysis data and
218 PIOMAS output, the TOPAZ4 SIT is thicker near the coast with ~ 50 cm (Fig. 1c), although the SIT
219 in the offshore region is underestimated. These positive and negative biases compensate each other
220 and thus the mean bias of the TOPAZ4 SIT is 21 cm in July, which is smaller than in winter (Table
221 3). The seasonal reduction of the SIT bias in TOPAZ4 is also found in the comparison between the
222 TOPAZ4 and CS2SMOS (Table 3). In fact, a similar positive bias emerges in comparison with the
223 climatological SIT in CS2SMOS in April (Fig. 2). It should be noted that a larger positive bias in
224 TOPAZ4 is located solely in the region of the Beaufort Gyre, with about 50 cm excess thickness
225 (Fig. 1c and 2c). Since in this region, both SIT data sets show some negative bias relative to the
226 independent SIT estimates derived from U.S. submarine data [Schweiger et al. 2011] and airborne
227 electromagnetic induction (EM) thickness measurements [Ricker et al. 2017], this positive bias may
228 be partly related to the underestimation of PIOMAS and CS2SMOS SITs, themselves.

229 Figure 3 shows the time series of daily mean SIT derived from PIOMAS and TOPAZ4
230 reanalysis and 7-days mean SIT derived from CS2SMOS, averaged over the ESS (70° – 80° N,
231 150° – 180° E, shown in Fig. 1a). The TOPAZ4 SIT data are reasonably similar to the seasonal cycle
232 of PIOMAS and CS2SMOS data with maxima in April–May and minima in October–November. In

233 particular, the TOPAZ4 SIT is within the standard deviation of PIOMAS SIT anomaly in each grid
234 relative to the area-averaged value in early summer (June-July). The monthly mean biases of
235 TOPAZ4 SIT data relative to PIOMAS in June and July are smaller than those in March to May
236 (Table 3). It should be noted that the TOPAZ4 SIT data in 2011 are strongly underestimated in early
237 summer. This might be related to the persistence of the negative bias until 2010 [Xie et al., 2017].

238 In the freezing season, the TOPAZ4 SIT in the ESS tends to be thinner than the PIOMAS SIT,
239 and seems comparable to the CS2SMOS SIT. The monthly mean bias of TOPAZ4 SIT relative to
240 CS2SMOS SIT is -23 cm and 1 cm in March and April, respectively (Table 3). On the other hand,
241 we should pay attention to the possibility that the CS2SMOS SIT may be underestimated in this
242 region, because the CS2SMOS highly depends on the reliability of merging two SIT data, which are
243 CryoSat-2 and SMOS SIT products [Ricker et al. 2017]. To check the possibility that the CS2SMOS
244 SIT has a negative bias in this area, we briefly examined the ice type data which were used for the
245 determination of merged SIT products. In the period from 2011 to 2013, the uncertainty of
246 CS2SMOS SIT is out of range for that of PIOMAS, but the CS2SMOS SIT is comparable to that for
247 PIOMAS in 2014 when the sea ice is classified as multi-year ice (Fig. 3). This result implies that the
248 CS2SMOS SIT is underestimated in the ESS due to the large fraction of SMOS SIT products even
249 in the sea ice thicker than 1 m.

250 Finally, we compared the SIT data in TOPAZ4 with the in-situ observations available in and
251 around the ESS. Although the location of these buoy data are not fully delimited in the ESS focused
252 in this study the ESS on which we focused in this study, these data seem to be appropriate for our
253 purpose, because the range of the climatological SIT in these region is similar to that in the ESS
254 (Fig. 1a). The direct comparison between the TOPAZ4 and IMB shows that the mean bias and root
255 mean square error of TOPAZ4 is 8.3 cm and 30 cm, respectively (Fig. 4). In particular, the TOPAZ4
256 SIT data shows a good correspondence with IMB buoy data in 2014, which is near the ESS in July
257 (Fig. 1a and Table 1). These results support the reliability of TOPAZ4 SIT data in the ESS in early

258 summer. Thus, at least the overall spatial distribution of SIT in the ESS is qualitatively simulated in
259 the TOPAZ4 and the inherent negative bias is suppressed in early summer, which is partly related to
260 the compensation by the positive bias near the shelf region of the ESS.

261

262 **4. Medium-range forecast skill of SIT distribution in the ESS**

263 In this section, we evaluate the prediction skill of SIT based on the PCCs between the analysis
264 and predicted data in the ESS. However, before this evaluation, we examine the mean fields and the
265 variability of the SIT and SIC distributions in early summer. Figure 5a presents the spatial
266 distribution of the climatological SIT and SIC in July, which shows that relatively thick sea ice (~1
267 m) covers 50%–70% of the ESS. Along the zone of the sea ice edge, the temporal standard
268 deviation of the daily mean SIT anomaly is relatively large with the maximum value of 0.6 m in the
269 coastal region (Fig. 5b) and the area-averaged value is maximum in July–August (Fig. 5c). Since
270 the SIT reduction rate in the ESS is strongest in these months (Fig. 5c) and the storm activity is
271 prevalent for periods of several days [Orsolini and Sorteberg, 2009], it is likely that dynamical and
272 thermodynamically-induced SIT variations are large. Note that the RMS of the SIC anomaly
273 averaged over the ESS also shows a similar seasonal cycle (not shown). Thus, it is meaningful to
274 examine the medium-range predictability of early summer SIT distribution in the ESS.

275 Figure 6a shows the seasonal dependency of PCC between the predicted and analyzed SIT at
276 lead times of 0–9 days. We found that the overall prediction skill is relatively low in warm season
277 (June-September) with a larger spread compared with the cold season (October–May). This result is
278 roughly consistent with the larger variance of the SIT anomaly in the warm season in the ESS (Fig.
279 5c). A large portion of the prediction skill at the lead times of 0–3 days can be explained by the
280 persistency effect based on the initial SIT (Fig. 6b). The contribution of the operational model on
281 the forecast skill is less than 5% at shorter timescale (<3 days) (Fig. 6c), but the contribution of the
282 operational model gradually increases at longer lead times except in May and October. In July, the

283 contribution of the operational model on the prediction skill reaches ~15% at 7 day lead time. These
284 results indicate that the operational model substantially improves the medium-range prediction skill
285 of the SIT distribution in summer.

286 Figure 7a shows the PCC of SIT distribution averaged in early summer (June–July). The SIT
287 distribution is predicted skillfully for a lead time of up to 3 days (Fig. 7a); however, the prediction
288 skill decreases abruptly at a lead time of 4 days, in which the standard deviation is also relatively
289 large. Such an abrupt reduction of the prediction skill and the enhanced standard deviation are also
290 found in May and September, although the absolute values of the reduction rates are smaller than in
291 July. Since the influence of sea ice melt is small in these months (Fig. 5c), the abrupt reduction of
292 early summer SIT prediction skill might be attributable to dynamical advection of sea ice.

293 To examine the influence of dynamical processes on the prediction skill of early summer SIT
294 distribution, we consider the prediction skill of sea ice velocities and surface wind velocities. The
295 prediction skill of sea ice velocity stays on a high level (>0.8) with small spread for a lead time of
296 up to 3 days, but decreases down to 0.6–0.7 for a lead time of 4 days (Fig. 7b). The early summer
297 prediction skill of surface wind speed also shows the same abrupt decrease at a lead time of 4 days,
298 and the rate of decrease of prediction skill is larger in meridional direction (Fig. 7c). Since the SIT
299 distribution has a tongue-like distribution (Fig. 5a), it is suggested that the meridional component of
300 SIT advection is sensitive to the sea ice transport in ice-edges, which influences the SIT distribution
301 in the ESS. These results confirm that the prediction skills of the sea ice velocities are strongly
302 related to those of surface wind speeds in the ESS.

303 Figure 8 shows the temporal evolutions of SIT and ice velocity for analysis and a forecast
304 bulletin starting from 2nd July 2015, which is a typical case of the abrupt decrease in the prediction
305 skill of SIT as well as sea ice velocities for a lead time of 4 days (Fig. 8; lower panel). For lead
306 times of +0 (2 July) to +2 days (4 July), the spatial distributions of SIT and ice velocity are
307 predicted skillfully with only small differences between them (Fig. 8; right panels). At a lead time

308 of +4 days (6 July), the analyzed sea ice velocity is directed northwestward in the ESS, which is
 309 related to the cyclonic circulation over the Novosibirsk Islands; however, the predicted sea ice
 310 velocity is directed southwestward. At a lead time of +6 days, the predicted and analyzed sea ice
 311 velocities are largely unrelated. The resultant onshore anomaly of sea ice velocity leads to positive
 312 and negative anomalies in SIT in the coastal and offshore regions, respectively. We also examined
 313 the time evolutions of the surface wind velocities in the atmospheric forecast data, and found them
 314 very similar to the sea ice velocity fields (not shown). These results indicate that the abrupt
 315 reduction of the prediction skill of early summer SIT in the ESS is related to a deficiency in the
 316 prediction of Arctic cyclone formation.

317 Further, we examine diagnostically the ice drift speed and direction based on a classical
 318 free-drift theory [Leppäranta, 2005], using the sea ice speed of TOPAZ4 reanalysis data and ERA
 319 interim atmospheric wind data in July 2011–2014. The general solution of sea ice speed (u) can be
 320 described as complex numbers:

$$321 \quad u = \alpha e^{-i\theta} U_a + U_{wg} \quad (2)$$

322 where U_a , and U_{wg} are the wind speed and geostrophic water velocities, respectively. The terms α
 323 and θ are the wind factor and the deviation angle of ice motion from the surface wind, respectively,
 324 where a positive angle is in counterclockwise direction. If we neglect the geostrophic water velocity
 325 U_{wg} , the wind factor and deviation angle can be obtained in the following form:

$$326 \quad \alpha^4 + 2 \sin \theta_w RNa \alpha^3 + R^2 Na^2 \alpha^2 - Na^4 = 0, \quad (3)$$

$$327 \quad \theta = \arctan \left(\tan \theta_w + \frac{RNa}{\alpha \cos \theta_w} \right) - \theta_a, \quad (4)$$

328 where θ_w and θ_a are the boundary layer turning angles of water and air, respectively. The turning
 329 angle θ is the angle between the vectors of the ice–water stress and the sea ice motion, which is a
 330 consequence of the viscous effect within the ocean boundary layer. The Nansen number Na is

331 defined by $\sqrt{\rho_a C_a / \rho_w C_w}$, where ρ_a and ρ_w represent the density of air and water, respectively, and
332 C_a and C_w are air and water drag coefficients, respectively. The Rossby number R is defined by
333 $(\rho h_{ice} f) / (\rho_w C_w N a |U_a|)$, where ρ is the ice density, f is the Coriolis parameter, and $|U_a|$ is the speed
334 of the surface wind. To calculate the wind factor α and the deviation angle θ under a given surface
335 wind speed, we used constant parameters of $C_a = 1.2 \times 10^{-3}$, $C_w = 5 \times 10^{-3}$, $\rho_a = 1.3 \text{ kg m}^{-3}$, $\rho_w =$
336 1026 kg m^{-3} , $\rho = 910 \text{ kg m}^{-3}$, $f = 1.3 \times 10^{-4} \text{ s}^{-1}$, and $\theta_w = 20^\circ$, which are values typical of the Arctic
337 Ocean [McPhee, 2012]. The value of α was calculated numerically from a 4th-order polynomial (Eq.
338 (3)).

339 On a first order approximation, the daily mean sea ice speed is linearly proportional to the
340 surface wind speed (10-m height) averaged over a part of the ESS (Fig. 9a). The correlation
341 between them is 0.96, which is significant at the 99% confidence level, based on the Monte Carlo
342 simulation [Kaplan and Glass, 1995]. The regression coefficient of ice speed onto the 10-m wind
343 speed is 0.022, which is consistent with the well-known 2% relationship between the speed of ice
344 and the surface wind speed [Thorndike and Colony, 1982]. The number of the TOPAZ4 ice speed
345 data within $\pm 20\%$ of the theoretical value is 79 days, which accounts for 63% of the total analyzed
346 period. Note that the observed regression coefficient is somewhat larger than the theoretical value
347 (0.018) averaged over the range of surface wind speed of 2–10 m s^{-1} calculated from Eq. (2). Since
348 the classical free drift theory [Leppäranta, 2005] neglects both the Ekman layer velocity and the
349 ocean geostrophic velocity, the absence of an ice-ocean boundary layer is likely to underestimate
350 the wind-induced ice velocity [Park and Stewart, 2016]. The deviation angle of sea ice motion in
351 TOPAZ4 is estimated as 20° – 40° under a wind condition $> 5 \text{ m s}^{-1}$, but it gradually increases to
352 40° – 70° under weaker wind conditions of $< 5 \text{ m s}^{-1}$ (Fig. 9b). The decrease of the deviation angle as
353 the surface wind strengthens is also consistent with earlier studies [Thorndike and Colony, 1982].
354 These observed deviation angles are comparable with their theoretical values calculated using Eq.

355 (4). The finding that the estimated values of the wind factor and the deviation angle are
356 approximately within the range of typical surface wind parameters (i.e., 2% for the wind factor and
357 30° for the deviation angle) in the Arctic Ocean confirms that sea ice velocity in the ESS is
358 controlled predominantly by wind stress drag: thus, the influence of ocean currents is not essential.

359 It is interesting that the prediction skill of SIT in early summer remains ~0.9 for the PCC core
360 at the lead times longer than 4 days (Fig. 7a), despite the poorer prediction skill of sea ice velocity
361 (Fig. 7b). This suggests that the SIT prediction skill after a lead time of 4 days is not strongly
362 attributed to the dynamical process but rather the thermodynamic process (i.e., the melting process
363 of sea ice). To evaluate the effect of sea ice melting on SIT prediction skill, we roughly estimated
364 the thermodynamic SIT change based on a simple sea ice melting model, as follows:

$$365 \quad h^p(t) = h^a(t_0) + \Delta t \times d\bar{h} / dt \quad (5)$$

366 where h^p is the predicted thermodynamic SIT change, h^a is the initial condition, which is
367 derived from the analysis SIT, and $d\bar{h} / dt$ is the rate of reduction of SIT due to sea ice melting. It
368 is known that the summertime surface heat flux in the Pacific sector of the Arctic Ocean is
369 dominated by the shortwave radiation flux [Perovich et al. 2007; Steele et al. 2008]. Recently, the
370 seasonal evolution of sea ice retreat in early summer has been found to be explained well by a
371 simplified ice–ocean coupled model, in which shortwave radiation is assumed constant [Kashiwase
372 et al. 2017]. Therefore, as the melting rate of the SIT in each year, we used the reduction rate of SIT
373 calculated from the climatological analysis SIT data during 2013–2016, which is likely to reflect the
374 typical thermodynamic melting rate in recent years and the SIT change due to transient sea ice
375 advection seems to be negligible. Here, we also evaluate the prediction skill of the persistency in the
376 initial SIT in the ESS (first term of the RHS in Eq. (5)).

377 Figure 10 shows the prediction skills of early summer SIT distribution in the ESS based on the
378 simple sea ice melting and persistency models. The prediction skill of the simple melting model,

379 which is lower than the full physics model, is very similar to that of the persistency model up to 3
380 days. However, the prediction skill of the simple melting model is comparable with that of the full
381 physics model after a lead time of 4 days, which is higher than that of persistency. Figure 11 shows
382 the temporal evolutions of SIT difference between the forecast and analysis data in each prediction
383 model in the period 2–9 July 2015. From the lower panel of Fig. 11, we found that the prediction
384 skill of the full physics model is higher than the simple melting and persistency models for lead
385 times of 0–5 days, but comparable with the prediction skill of the simple melting model at longer
386 lead times (> 6 days). In the SIT difference map of the full-physics model minus the operational
387 analysis, a positive anomaly (i.e., overestimation of SIT), is evident along the sea ice edge at a lead
388 time of 4 days, and then gradually increases until a lead time of 8 days. For the case of the simple
389 melting model, a similar positive anomaly emerges at a lead time of 4 days, but the positive
390 anomaly appears stationary along the coastal region, compared to the full physics model. The
391 persistency model overestimates SIT over the entire region during the prediction. These results
392 support the idea that the melting process is important in the prediction of early summer SIT over
393 longer timescales.

394

395 **5. Case study of ice-blocked incident in the ESS in July 2014**

396 In the perspective of operational application of the TOPAZ4 sea ice data to the maritime
397 navigation of the NSR, we briefly examine the relationship between the sea ice conditions and AIS
398 vessel speed data for the case of an ice-blocking incident involving two vessels, based on the
399 TOPAZ4 reanalysis data. Figure 12 shows the vessel tracks during July 4–30 2014, when the two
400 vessels became blocked in the ESS for about one week. During this period, SIT in excess of 100 cm
401 is found in the ESS with the maximum thickness of 150 cm. A joint statistical analysis of the daily
402 mean SIT in the TOPAZ4 reanalysis and the vessel speed along the route indicates that vessel speed
403 is significantly anticorrelated with SIT (-0.56) during the entire passage (Fig. 13a), significant at

404 the 99 % confidence level based on a Monte Carlo technique [Kaplan and Glass, 1995]. We also
405 examined the corresponding SIC data in TOPAZ4 reanalysis data, but the correlation between the
406 vessel speed and SIC is -0.41 (Fig. 13b), which is insignificant at 99% confidence level. The scatter
407 plots for SIC indicates that the SIC value is partly insensitive to the vessel speed higher than 5 knot.
408 Thus, these results suggest that the vessel speed was influenced by sea ice stress due to SIT and
409 indirectly supports the reliability of the daily mean SIT of the TOPAZ4 reanalysis data in the ESS
410 in early summer.

411

412 **6. Summary and discussion**

413 In this study, the medium-range forecast skill of early summer SIT distribution in the ESS was
414 evaluated using the TOPAZ4 data assimilation system. Comparisons between the operational model,
415 observed, and TOPAZ4 reanalysis SIT data showed that the TOPAZ4 reanalysis qualitatively
416 reproduces the tongue-like distribution of SIT in the ESS in early summer, and its seasonal variation
417 (maximum in April–May and minimum in October–November) including the rates of advance and
418 melting of sea ice in the ESS). Although in this region, the inherent negative bias of SIT in TOPAZ4
419 is relatively large in March to May, the bias is reduced in early summer (June–July) within $\sim\pm 20$ cm
420 due to the excess of SIT along the coastal region in the ESS. The TOPAZ4 SIT data also shows a
421 good correspondence with IMB buoy data in and around the ESS with the mean bias of ~ 9 cm and
422 the root mean square error of ~ 30 cm. Thus, the TOPAZ4 SIT data could be considered reliable
423 estimates for the ESS even in the absence of satellite observations in summer.

424 For the positive bias of the SIT in TOPAZ4 along the coastal region of the ESS, there is a
425 possibility that the SIT estimates (PIOMAS and CS2SMOS) used for the comparison are
426 themselves underestimated. Schweiger et al. [2011] pointed out that the SIT of PIOMAS is
427 underestimated by -17cm in the basin area of the Arctic Ocean including the Beaufort Sea where the
428 heavy deformed sea ice formation occurs. Also, it was reported that the CS2SMOS SIT data tend to

429 underestimate SIT in regions where multi-year ice and first-year ice are formed, due to the relative
430 accuracy of CryoSat-2 and SMOS and the merging algorithm [Ricker et al. 2017]. Since in the ESS,
431 sea ice motion is strongly converging during winter [Kimura et al. 2013], there is a possibility that
432 the sea ice in the ESS is also heavily deformed to form sea ice thicker than 1 m along the coastal
433 region. In fact, our analysis based on the AIS data suggests that SIT in excess of 100 cm is found
434 near the coast of the ESS. Thus, for a precise evaluation of the SIT distribution in the ESS, the
435 further improvement of ice-type as well as denser in-situ SIT measurements are needed.

436 The prediction skill of the SIT distribution in the TOPAZ4 forecast system was examined in
437 the ESS using a pattern correlation analysis. Although the prediction skill was relatively lower in
438 early summer (June–July) with a large spread, the SIT distribution was predicted skillfully for a
439 lead time of up to 3 days, and the prediction skill drops abruptly after the 4th day. A similar change
440 in prediction skill was also found for sea ice velocity and surface wind speed over the ESS.
441 Diagnostic analysis of the sea ice velocity variability revealed that the early summer ice speed and
442 direction over the EES could be explained well by the free-drift mechanism with a wind factor of
443 2.2 % and a deviation angle of 30°–50°. Their results suggested that the large reduction of
444 prediction skill could be attributed to the process of dynamical advection of sea ice; thus, the
445 prediction of early summer SIT distribution will depend on precise prediction of the surface wind.
446 Our comprehensive analysis supports an earlier study that suggested the dynamical processes have
447 an essential role in the prediction skill of sea ice distribution on short timescales [Ono et al., 2016].

448 The time evolution of SIT and the related ice velocity relates the large difference between the
449 forecast and analysis data at a lead time of 4 days to the low forecast skills for an Arctic cyclone
450 event. Jung and Matsueda [2017] highlighted that large-scale atmospheric fluctuations in the Arctic
451 region in winter are predicted skillfully for lead times of up to 5 days in the operational forecast
452 system, which is very similar to the prediction skill in mid-latitude regions. However, Yamagami et
453 al. [2018] reported that the skillful prediction of Arctic cyclones generated in summer is limited to 4

454 days, which is shorter than the case for the mid-latitudes [Froude, 2010]. As this area is located near
455 the transit zone of summertime storm tracks generated over Eurasia [Serreze and Barry, 1988], the
456 predictability of Arctic cyclones could be an important factor in the determination of the lead time
457 of surface wind speed and thus, of the SIT distribution in the ESS. The low prediction skill of the
458 meridional wind and ice speed suggested that the meridional component of sea ice advection
459 contributes substantially to the SIT distribution in the ESS. Since it was reported that additional
460 radiosonde observations over the Arctic Ocean have considerable impact on the prediction skill in
461 synoptic-scale fluctuations [Inoue et al., 2015; Yamazaki et al., 2015], additional radiosonde
462 observations acquired over the Arctic Ocean could lead to further extension of the lead time for
463 medium-range forecast skill of SIT distribution.

464 Based on sensitivity experiments using a simple melting and a persistency model, it was found
465 that the longer timescale prediction of SIT in early summer could be attributed to the
466 thermodynamic melting process. As the shortwave radiation flux is maximum in early summer
467 (June–July), the change of SIT due to the advection in relation to synoptic-scale atmospheric
468 fluctuations is likely to be smaller than the thermodynamic SIT reduction along the sea ice edge.
469 Although the recognition of the importance of the thermodynamic melting process on sea ice
470 prediction on seasonal timescales has been pointed out by earlier studies [Kimura et al. 2013;
471 Bushuk et al. 2017; Kashiwase et al. 2017], our study clarified that the influence has a substantial
472 role on the medium-range forecast of early summer SIT distribution. Thus, the influence of sea ice
473 advection on early summer sea ice prediction is limited to a lead time of 4–5 days, but is dominated
474 by the thermodynamic melting process in later stage of the lead times. In other words, the SIT
475 prediction skill in early summer is not necessarily worse at the longer timescale. It is noteworthy
476 that the dynamical process is not unimportant for the long-term prediction in the SIT distribution in
477 early summer, because the skillful prediction skill at a lead time of 3 days is important as the initial
478 conditions for the melting process dominated for a lead time longer than 4 days. Thus, it is

479 concluded that the atmospheric prediction skill for a lead time of up to 3 days contributes to the
480 short and medium-range prediction skill of the SIT distribution in early summer.

481 In view of the operational application of the TOPAZ4 sea ice data to the navigation in NSR,
482 this study found that during an ice-blocking event that affected two tankers in the ESS in July 2014,
483 significant SIT (~150 cm) was simulated over the ESS by TOPAZ4. Given that the SIT is found to
484 be underestimated by 20 cm in TOPAZ4, the true SIT is expected to be above 150 cm. Statistical
485 analysis suggested that vessel speed was significantly anticorrelated with the daily mean SIT
486 variations (-0.56) rather than the SIC (-0.41). This result demonstrated the reliability of the early
487 summer SIT distribution in the TOPAZ4 reanalysis data and its high potential for operational use in
488 support of maritime navigation of the NSR. However, this result was only based on a case study of
489 two ships in July 2014. To clarify the determinant factor on vessel speed, comprehensive statistical
490 analysis will be needed based on the speed data of different types of vessel.

491 Future projections for storm track activity (intensity and number) under the scenario of Arctic
492 climate change have been addressed by several researchers. For example, based on control
493 experiments using climate models, Bengtsson et al. [2006] found that summertime storm activity is
494 expected to increase. Orsolini and Sorteberg [2009] found that the number of storms, particularly
495 along the Eurasian Arctic coast, could increase in the future, because of the local enhancement of
496 the meridional temperature gradient between the Arctic Ocean and the warmed Eurasian continent.
497 Nishii et al. [2015] supported that their findings based on analyses using the CMIP3 and CMIP5
498 global climate model simulations, although they highlighted that the CMIP projections had
499 considerable uncertainty. Thus, further investigations of the formation and the development
500 mechanisms of summertime Arctic cyclones are needed for the improvement of the prediction skill
501 of atmospheric wind conditions, which are responsible for the forecast skill of early summer sea ice
502 distribution over 4 days.

503

504 **Acknowledgements**

505 The AMSR2 brightness temperatures and products data were provided by the Japan Aerospace
506 Exploration Agency (JAXA). The dataset of AMSR2 SIT and SIC was archived and provided by the
507 Arctic Data archive System (ADS), which was developed by the National Institute of Polar
508 Research (NIPR). The merging of CryoSat-2 und SMOS data was funded by the ESA project
509 SMOS+ Sea Ice (4000101476/10/NL/CT and 4000112022/14/I-AM) and data from 2010 to 2014
510 were obtained from <http://www.meereisportal.de> (Grant No.: REKLIM-2013-04). The ECMWF
511 atmospheric forecast data were provided by the ECMWF TIGGE portal site via the TIGGE medium
512 of the University of Tsukuba (<http://gpvjma.ccs.hpcc.jp/TIGGE/>). The TOPAZ4 forecast data were
513 analyzed using the Pan-Okhotsk Information System of ILTS. This work was supported by Arctic
514 Challenge for Sustainability (ArCS) project of the Ministry of Education, Culture, Sports, Science
515 and Technology in Japan, and JSPS KAKENHI Grant Numbers JP17KK0014, JP18H0374. We
516 thank James Buxton MSc from Edanz Group ([www.edanzediting.com./ac](http://www.edanzediting.com/ac)) for correcting a draft of
517 this manuscript.

518

519 **References**

- 520 Barnett T. P., & Schlesinger M. E. 1987. Detecting changes in global climate induced by
521 greenhouse gases. *J. Geophys. Res.* 92, 14772–14780, doi:10.1029/JD092iD12p14772.
- 522 Bengtsson L., Hodges K.I., & Roeckner E. 2006. Storm Tracks and Climate Change. *J. Climate* 19,
523 3518–3543, <https://doi.org/10.1175/JCLI3815.1>.
- 524 Blanchard-Wrigglesworth E. & Bitz, C. M. 2014. Characteristics of Arctic Sea-Ice Thickness
525 Variability in GCMs. *J. Climate* 27, 8244–8258.
- 526 Bushuk M., Msadek R., Winton M., Vecchi G. A., Gudgel R., Rosati A., & Yang X. 2017. Skillful
527 regional prediction of Arctic sea ice on seasonal timescales. *Geophys. Res. Lett.* 44,
528 doi:10.1002/2017GL073155.
- 529 Cavalieri D. J. & Parkinson C. L. 2008. Arctic sea ice variability and trends, 1979–2006. *J.*
530 *Geophys. Res.* 113, C07003, doi:10.1029/2007JC004558.
- 531 Chen Z., Liu J., Song M., Yang Q., & Xu S. 2017. Impacts of Assimilating Satellite Sea Ice
532 Concentration and Thickness on Arctic Sea Ice Prediction in the NCEP Climate Forecast
533 System. *J. Climate* 30, 8429–8446.
- 534 Collow T., Wang W., Kumar A., & Zhang J. 2015. Improving Arctic Sea Ice Prediction Using
535 PIOMAS Initial Sea Ice Thickness in a Coupled Ocean–Atmosphere Model. *Mon. Wea. Rev.*
536 143, 4618–4630, doi: 10.1175/MWR-D-15-0097.1.
- 537 Comiso J. C. 2012. Large Decadal Decline of the Arctic Multiyear Ice Cover. *J. Climate* 25, 1176–
538 1193, <https://doi.org/10.1175/JCLI-D-11-00113.1>.
- 539 Dee D. P. et al. 2011. The ERA-Interim reanalysis: configuration and performance of the data
540 assimilation system. *Q.J.R. Meteorol. Soc.* 137, 553–597. doi: 10.1002/qj.828.
- 541 Eguíluz V. M., Fernández-Gracia J., Irigoien X., & Duarte C. M. 2016. A quantitative assessment
542 of Arctic shipping in 2010–2014. *Sci. Rep.* 6, 30682, doi:10.1038/srep30682.
- 543 Fichetfet T., & Maqueda M. A. M. 1997. Sensitivity of a global sea ice model to the treatment of ice

544 thermodynamics and dynamics. *J. Geophys. Res.* 102, 12609–12646, doi:10.1029/97JC00480.

545 Froude L. S. R. 2010. TIGGE: Comparison of the prediction of Northern Hemisphere extratropical
546 cyclones by different ensemble prediction systems. *Weather and Forecasting* 25, 819–836.
547 <https://doi.org/10.1175/2010WAF2222326.1>.

548 Grosfeld K., Treffeisen R., Asseng J., Bartsch A., Bräuer B., Fritsch B., Gerdes R., Hendricks S.,
549 Hiller W., Heygster G., Krumpen T., Lemke P., Melsheimer C., Nicolaus M., Ricker R., &
550 Weigelt M. 2016. Online sea-ice knowledge and data platform <www.meereisportal.de>,
551 Polarforschung, Bremerhaven, Alfred Wegener Institute for Polar and Marine Research &
552 German Society of Polar Research 85, 143-155, doi:10.2312/polfor.2016.011.

553 Holland M. M., Bailey, D. A. & Vavrus, S. 2011. Inherent sea ice predictability in the rapidly
554 changing Arctic environment of the Community Climate System Model, version 3. *Clim. Dyn.*
555 36, 1239–1253, doi:10.1007/s00382-010-0792-4.

556 Honda M., Inoue J., & Yamane S. 2009. Influence of low Arctic sea-ice minima on anomalously
557 cold Eurasian winters. *Geophys. Res. Lett.* 36, L08707, doi:10.1029/2008GL037079.

558 Hunke E. & Dukowicz J. 1997. An Elastic–Viscous–Plastic Model for Sea Ice Dynamics. *J. Phys.*
559 *Oceanogr.* 27, 1849–1867.

560 Inoue J., Hori M., & Takaya K. 2012. The role of Barents sea ice in the wintertime cyclone track
561 and emergence of a Warm-Arctic Cold Siberian anomaly. *J. Climate* 25, 2561-2568.

562 Inoue J., Yamazaki A., Ono J., Dethloff K., Maturilli M., Neuber R., Edwards P., & Yamaguchi H.
563 2015. Additional Arctic observations improve weather and sea-ice forecasts for the Northern
564 Sea Route. *Sci. Rep.* 5, 16868, doi:10.1038/srep1686.

565 JAXA 2013. Descriptions of GCOM-W1 AMSR2 Level 1R and Level 2 Algorithms, Rev. A.

566 Jung, T. & Matsueda, M. 2016. Verification of global numerical weather forecasting systems in
567 polar regions using TIGGE data. *Q.J.R. Meteorol. Soc.* 142: 574–582. doi: 10.1002/qj.2437.

568 Kaplan, D. & Glass L. 1995. *Understanding nonlinear dynamics*, Springer-Verlag, New York, pp.

569 420.

570 Kara A., Rochford P., & Hurlburt H. 2000. Efficient and Accurate Bulk Parameterizations of Air–
571 Sea Fluxes for Use in General Circulation Models. *J. Atmos. Oceanic Technol.* 17, 1421–1438.

572 Kashiwase H., Ohshima K. I., Nihashi S., & Eicken H. 2017. Evidence for ice-ocean albedo
573 feedback in the Arctic Ocean shifting to a seasonal ice zone. *Sci. Rep.* 7, 8170,
574 doi:10.1038/s41598-017-08467-z.

575 Kimura N., Nishimura A., Tanaka Y., & Yamaguchi H. 2013. Influence of winter sea-ice motion on
576 summer ice cover in the Arctic. *Polar Research* 1751-8369,
577 doi:http://dx.doi.org/10.3402/polar.v32i0.20193.

578 Large W.G. & Pond S. 1981. Open Ocean Momentum Flux Measurements in Moderate to Strong
579 Winds. *J. Phys. Oceanogr.* 11, 324–336.

580 Laxon S. W., Giles K. A., Ridout A. L., Wingham D. J., Willatt R., Cullen R., Kwok R., Schweiger
581 A., Zhang J., Haas C., Hendricks S., Krishfield R., Kurtz N., Farrell S. & Davidson M. 2013.
582 CryoSat-2 estimates of Arctic sea ice thickness and volume, *Geophys. Res. Lett.* 40, 732–737.

583 Leppäranta M. 2005. *The Drift of Sea Ice*. Springer-Verlang, 266 pp.

584 Lisæter K. A., Rosanova J., & Evensen G. 2003. Assimilation of ice concentration in a coupled
585 ice-ocean model, using the Ensemble Kalman filter. *Ocean Dynamics* 53, 368–388.
586 <http://doi.org/10.1007/s10236-003-0049-4>.

587 Lindsay R.W. & Zhang J. 2006. Arctic Ocean Ice Thickness: Modes of Variability and the Best
588 Locations from Which to Monitor Them. *J. Phys. Oceanogr.* 36, 496–506,
589 <https://doi.org/10.1175/JPO2861.1>.

590 Lindsay R. W., Zhang J., Schweiger A. J., & Steele M. A. 2008. Seasonal predictions of ice extent
591 in the Arctic Ocean. *J. Geophys. Res.* 113, C02023, doi:10.1029/2007JC004259.

592 McPhee M. G. 2012. Advances in understanding ice-ocean stress during and since AIDJEX. *Cold
593 Reg. Sci. Technol.* 76, 24-36.

- 594 Melia N., Haines K., & Hawkins E. 2015. Improved Arctic sea ice thickness projections using
595 bias-corrected CMIP5 simulations. *The Cryosphere* 9, 2237-2251,
596 doi:10.5194/tc-9-2237-2015.
- 597 Melia N., Haines K., & Hawkins E. 2016. Sea ice decline and 21st century trans-Arctic shipping
598 routes. *Geophys. Res. Lett.* 43, 9720–9728, doi:10.1002/2016GL069315.
- 599 Melia N., Haines K., Hawkins E., & Day J. J. 2017. Towards seasonal Arctic shipping route
600 predictions. *Env. Res. Lett.* 12, 084005.
- 601 Mori M., Watanabe M., Shiogama H., Inoue J., & Kimoto M. 2014. Robust Arctic sea-ice influence
602 on the frequent Eurasian cold winters in past decades. *Nat. Geosci.*, 7, 869–873.
- 603
- 604 Nishii K., Nakamura H., Orsolini Y. J. 2015. Arctic summer storm track in CMIP3/5 climate
605 models. *Clim. Dyn.* 44, 1311, <https://doi.org/10.1007/s00382-014-2229-y>.
- 606 Ono J., Inoue J., Yamazaki A., Dethloff K., & Yamaguchi H. 2016. The impact of radiosonde data
607 on forecasting sea-ice distribution along the Northern Sea Route during an extremely
608 developed cyclone. *J. Adv. Model Earth Syst.* 8, 292-303, doi:10.1002/2015MS000552.
- 609 Orsolini Y. J. & Sorteberg A. 2009. Projected changes in Eurasian and Arctic summer cyclones
610 under global warming in the Bergen climate model. *Atmos. Oceanic Sci. Lett.* 2, 62-67.
- 611 Overland J. E., Francis J. A., Hall R., Hanna E., Kim S.-J., & Vihma T. 2015. The melting Arctic
612 and mid-latitude weather patterns: Are they connected? *J. Climate*, 28, 7917-7932,
613 doi:10.1175/JCLI-D-14-00822.1.
- 614 Park H.-S. & Stewart A. L. 2016. An analytical model for wind-driven Arctic summer sea ice drift,
615 *The Cryosphere*, 10, 227–244.
- 616 Pastusiak T. 2016. *The Northern sea route as a shipping lane*. Springer, Swizerland, p. 219.
- 617 Perovich D. K., Light B., Eicken H., Jones K. F., Runcimen K., & Nghiem S. V. 2007. Increasing
618 solar heating of the Arctic Ocean and adjacent seas, 1979–2005: Attribution and the role of

619 ice-albedo feedback. *Geophys. Res. Lett.* 34, L19505, doi:10.1029/2007GL031480.

620 Perovich D., Richter-Menge J., Elder B., Arbetter T., Claffey K., & Polashenski C. 2013. Observing
621 and understanding climate change: Monitoring the mass balance, motion, and thickness of
622 Arctic sea ice. Cold Regions Research and Engineering Laboratory.
623 <http://www.imb-crrel-dartmouth.org/imb.creel>.

624 Persson A. 2011. User guide to ECMWF forecast products ver. 1.2, October 2011, ECMWF,
625 Reading, pp. 121.

626 Petoukhov V., & Semenov V. A. 2010. A link between reduced Barents-Kara sea ice and cold
627 winter extremes over northern continents. *J. Geophys. Res.* 115, D21111,
628 doi:10.1029/2009JD013568.

629 Ricker R., Hendricks S., Kaleschke L., Tian-Kunze X., King J., & Haas C. 2017. A weekly Arctic
630 sea-ice thickness data record from merged CryoSat-2 and SMOS satellite data. *The Cryosphere*
631 11, 1607-1623, <https://doi.org/10.5194/tc-11-1607-2017>.

632 Sakov P., & Oke P. R. 2008. A deterministic formulation of the ensemble Kalman filter: an
633 alternative to ensemble square root filters. *Tellus* 60A, 361–371.

634 Sakov P., Counillon F., Bertino L., Lisæter K. A., Oke P. R., & Korabely A. 2012. TOPAZ4: an
635 ocean-sea ice data assimilation system for the North Atlantic and Arctic. *Ocean Sci.* 8,
636 633-656, doi:10.5194/os-8-633-2012.

637 Sato K. & Inoue J. 2017. Comparison of Arctic sea ice thickness and snow depth estimates from
638 CFSR with in situ observations. *Clim. Dyn.* 1-13, doi:10.1007/s00382-017-3607-z.

639 Schøyen H., & Bråthen S. 2011. The Northern Sea route versus the Suez Canal: cases from bulk
640 shipping. *J. Transp. Geogr.* 19, 977–983.

641 Screen J. A. 2017. Simulated Atmospheric Response to Regional and Pan-Arctic Sea Ice Loss. *J.*
642 *Climate* 30, 3945–3962, <https://doi.org/10.1175/JCLI-D-16-0197.1>

643 Schweiger A., Lindsay R., Zhang J., Steele M., Stern H., & Kwok R. 2011. Uncertainty in modeled

644 Arctic sea ice volume. *J. Geophys. Res.* 116, C00D06, doi:10.1029/2011JC007084.

645 Schweiger A. J., & Zhang J. 2015. Accuracy of short-term sea ice drift forecasts using a coupled
646 ice-ocean model. *J. Geophys. Res. Oceans* 120, 7827–7841, doi:10.1002/2015JC011273.

647 Semtner A. 1976. A Model for the Thermodynamic Growth of Sea Ice in Numerical Investigations
648 of Climate. *J. Phys. Oceanogr.* 6, 379–389.

649 Serreze M. C. & Barry R. G. 1988. Synoptic activity in the Arctic basin, 1979–85. *J. Climate* 1,
650 1276–1295.

651 Serreze M. C. & Barrett A. P. 2008. The summer cyclone maximum over the central Arctic Ocean.
652 *J. Climate* 21, 1048–1065.

653 Simonsen M., Hackett B., Bertino L., Røed L. P., Waagbø G. A., Drivdal M., Sutherland G. 2017.
654 PRODUCT USER MANUAL For Arctic Ocean Physical and Bio Analysis and Forecasting
655 Products 5.5. EU, Copernicus Marine Service, <http://marine.copernicus.eu> pp. 56.

656 Simmonds I. & Rudeva I. 2012. The great Arctic cyclone of August 2012. *Geophys. Res. Lett.* 39,
657 L23709, <https://doi.org/10.1029/2012GL054259>.

658 Stark J. D., Ridley J., Martin M., & Hines A. 2008. Sea ice concentration and motion assimilation
659 in a sea ice–ocean model. *J. Geophys. Res.* 113, C05S91, doi:10.1029/2007JC004224.

660 Steele M. Ermold W., & Zhang J. 2008. Arctic Ocean surface warming trends over the past 100
661 years. *Geophys. Res. Lett.* 35, L02614, doi:10.1029/2007GL031651.

662 Stroeve J., Hamilton L. C., Bitz C. M., & Blanchard-Wrigglesworth E. 2014. Predicting September
663 sea ice: Ensemble skill of the SEARCH Sea Ice Outlook 2008–2013. *Geophys. Res. Lett.* 41,
664 2411–2418, doi:10.1002/2014GL059388.

665 Tan X., Su K., Riska K., & Moan T. 2013. A six-degrees-of-freedom numerical model for level ice–
666 ship interaction. *Cold Reg. Sci. Technol.* 92, 1–16, doi:10.1016/j.coldregions.2013.03.006.

667 Thorndike A. S. & Colony R. 1982. Sea ice motion in response to geostrophic winds. *J. Geophys.*
668 *Res.* 87, 5845–5852, doi:10.1029/JC087iC08p05845.

669 Wang W., Chen M., & Kumar A. 2013. Seasonal Prediction of Arctic Sea Ice Extent from a
670 Coupled Dynamical Forecast System. *Mon. Wea. Rev.* 141, 1375–1394, doi:
671 10.1175/MWR-D-12-00057.1.

672 Wang X., Key J., Kwok R., & Zhang J. 2016. Comparison of Arctic Sea ice thickness from
673 satellites, aircraft, and PIOMAS data. *Remote Sens.* 8, 713, doi:10.3390/rs8090713.

674 Wassmann P. 2011. Arctic marine ecosystems in an era of rapid climate change. *Prog. Oceanogr.* 90,
675 1–17.

676 Xie J., Bertino L., Counillon F., Lisæter K. A., & Sakov P. 2017. Quality assessment of the
677 TOPAZ4 reanalysis in the Arctic over the period 1991–2013. *Ocean Sci.* 13, 123–144,
678 doi:10.5194/os-13-123-2017.

679 Yamagami A., Matsueda M., & Tanaka H. L. 2017. Extreme Arctic cyclone in August 2016.
680 *Atmosph. Sci. Lett.* 18: 307–314. doi: 10.1002/asl.757.

681 Yamagami A., Matsueda M., & Tanaka H. L. 2018. Predictability of the 2012 great Arctic cyclone
682 on medium-range timescales, 15, 13-23, doi: 10.1016/j.polar.2018.01.002.

683 Yamamoto-Kawai M., McLaughlin F. A., & Carmack E. C. 2011. Effects of ocean acidification,
684 warming and melting of sea ice on aragonite saturation of the Canada Basin surface water.
685 *Geophys. Res. Lett.* 38, L03601, doi:10.1029/2010GL045501.

686 Yamazaki A., Inoue J., Dethloff K., Maturilli M., & König-Langlo G. 2015. Impact of radiosonde
687 observations on forecasting summertime Arctic cyclone formation. *J. Geophys. Res.* 120,
688 3249–3273, doi:10.1002/2014JD022925.

689 Zhang J. & Rothrock D. A. 2003. Modeling global sea ice with a thickness and enthalpy
690 distribution model in generalized curvilinear coordinates. *Mon. Wea. Rev.* 131, 681–697.

691

692 **Table 1.** List of observed and simulated sea ice thickness datasets

Data sources		Period	Spatial resolution	Time step
TOPAZ4	Reanalysis	2011–2014	12.5 km	Daily
	Forecast	2013–2016	12.5 km	Daily
CS2SMOS		2011–2014 (October to April)	~25 km	7 days
IMB	2011K	1 September 2011 to 14 May 2012	Point-wise	Hourly
	2012I	14 August 2012 to 21 December 2012		
	2012J	25 August 2012 to 3 August 2013		
	2014B	26 March to 29 July 2014		
PIOMAS		2011–2014	~0.8°	Daily

693

694 **Table 2.** Pattern correlations of monthly mean climatologies of SIT in TOPAZ4 with those in
695 PIOMAS and CS2SMOS over the Arctic marginal seas (Laptev, East Siberian, and Chukchi Seas)

Month	Mar.	Apr.	May	Jun.	Jul.
PIOMAS	0.92	0.93	0.93	0.92	0.92
CS2SMOS	0.86	0.82	–	–	–

696

697 **Table 3.** Monthly mean biases of TOPAZ4 SIT in the ESS relative to the CS2SMOS and PIOMAS
698 SIT data

SIT bias (cm)	Mar.	Apr.	May	Jun.	Jul.
CS2SMOS	-23	<1	-	-	-
PIOMAS	-65	-63	-56	-23	21

699

700 **Figure captions**

701 **Figure 1.** Spatial distribution of climatological monthly mean of SIT (cm) in July during 2011–
702 2014: (a) PIOMAS, (b) TOPAZ4 reanalysis, and (c) their difference (cm). The boundaries of the
703 ESS and Arctic marginal seas are indicated in panel a by thick and thin lines, respectively. In panel
704 a, the trajectories of IMB buoys for 2011K, 2012I, 2012J, and 2014B (see Table 1 for the details of
705 each buoy data) are shown by black, red, blue and green dots, respectively.

706 **Figure 2.** Spatial distribution of climatological monthly mean of SIT (cm) in April during 2011–
707 2014: (top) CS2SMOS, (middle) TOPAZ4 reanalysis, and (bottom) their difference (cm).

708 **Figure 3.** Time series of daily mean SIT (cm) averaged over the ESS (rectangular region denoted
709 by black line in Fig. 1 (a)) derived from CS2SMOS (black), TOPAZ4 reanalysis (red), and
710 PIOMAS (blue) from January 2011 to August 2014. For CS2SMOS data, 7 day mean values are
711 shown. The standard deviations of area-averaged data are shown by vertical lines, respectively. The
712 ice types (2: first-year ice, 3: multi-year ice) used for the choice of satellite SIT retrievals in
713 CS2SMOS are shown by green bar. The scale for the ice type is located on the right vertical axis.

714 **Figure 4.** The comparisons of the daily mean SITs derived from IMB buoy data with the
715 corresponding SIT in TOPAZ4 reanalysis data from 2011 to 2014 in and around the ESS. The SIT
716 data are re-sampled per 7 days. The regression lines onto IMB buoy data and the reference unit line
717 are shown by solid and dashed lines, respectively.

718 **Figure 5.** Spatial distribution of (a) monthly mean (colors) climatological SIT (m) in the TOPAZ4
719 reanalysis and (b) the RMS variability of daily mean SIT (colors) in July during 2011–2014. The
720 monthly mean of climatological SIC (white contours) in July is indicated in panel (a). The
721 rectangular region enclosing the ESS (70° – 80° N, 150° – 180° E) is shown in panel (b). (c) Time
722 series of monthly mean SIT (grey shade) and RMS of TOPAZ4 reanalysis (black line) averaged
723 over the ESS. The scale of the RMS is indicated on the right axis.

724 **Figure 6.** The prediction skill (PCC) of SIT forecast in the ESS (70° – 80° N, 150° – 180° E) in each

725 month obtained from (a) operational forecast model and (b) persistency of the initial value,
726 averaged from 2014–2016. The standard deviations of the PCCs are shown with white contours. In
727 panel c, the fraction of variance explained by operational forecast relative to the persistency (%) is
728 shown by contour (the region where the fraction is larger than 10% is shaded).

729 **Figure 7.** PCCs between forecast and analysis (a) SIT, (b) zonal and meridional ice speed, and (c)
730 zonal and meridional surface wind speed from operational TOPAZ4 data in early summer
731 (June–July) averaged on 2014–2016. Error bar indicates the standard deviation of the PCCs.

732 **Figure 8.** Temporal evolution of SIT (cm; colors) and ice velocity (m s^{-1} ; vectors) distribution for
733 (left) analysis, (center) forecast, and (right) the difference between forecast and analysis at
734 increasing lead times from +0 day to +6 days initialized on 2nd July 2015. The corresponding PCCs
735 for the SIT (black), zonal (red) and meridional ice speeds (blue) in the ESS (right-lower panel of the
736 time evolution) are shown in the lower panel. The scale for the PCCs of the zonal and meridional
737 ice speeds is indicated on the right axis.

738 **Figure 9.** (a) Relationship between 10m wind speed (m s^{-1}) in the ERA Interim reanalysis data and
739 sea ice speed (m s^{-1}) in the TOPAZ4 reanalysis averaged over a part of the ESS (72° – 76° N,
740 150° – 170° E) during 1–31 July 2011–2014. Broken and solid lines indicate the regression line of
741 ice speed on 10m wind speed ($y = 0.0224x - 0.0112$) and the theoretical ice speed estimated based
742 on classical free-drift theory, respectively. (b) Angle (degrees) of sea ice velocity relative to surface
743 wind vectors averaged over the ESS. Positive values indicate sea ice drift is to the right of the wind
744 direction. Solid curve indicates the wind–ice velocity angle estimated based on classical free-drift
745 theory.

746 **Figure 10.** The PCCs between forecast and analysis SIT from the full physics model (black),
747 persistency (red), and a simple melting model (blue) in early summer (June–July) averaged from
748 2014–2016. Error bar indicates the standard deviation of the PCCs.

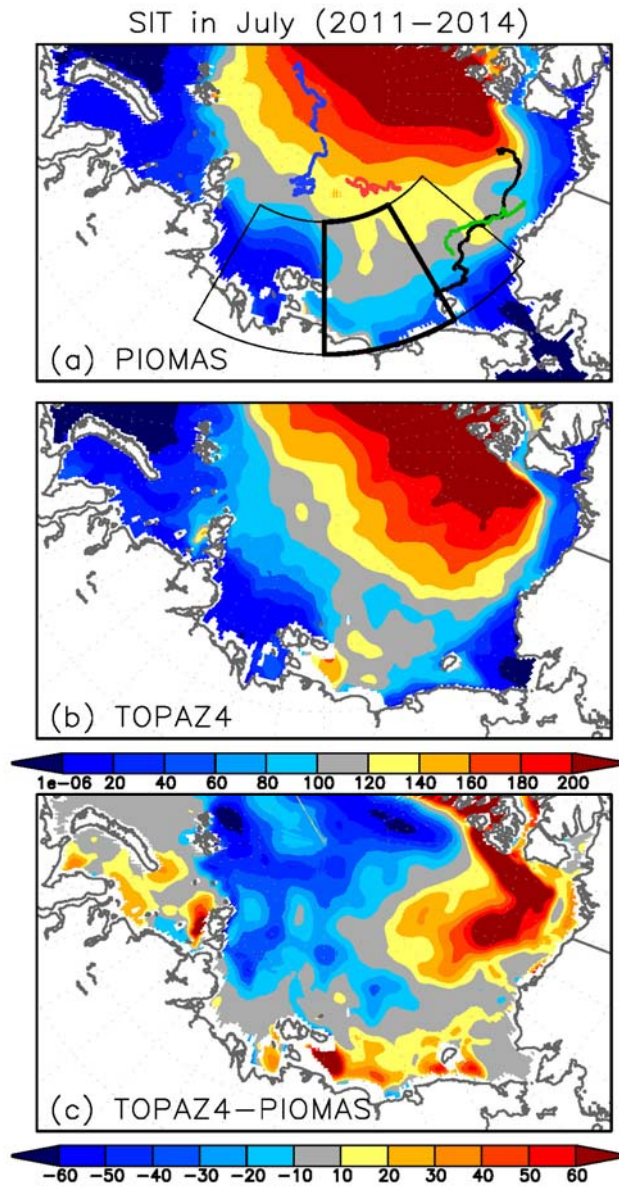
749 **Figure 11.** Temporal evolution of SIT differences (cm; colors) between the forecast and analysis

750 data at lead times increasing from +2 to +8 days, initialized on 2nd July 2015. In each panel, the sea
751 ice edge of the analysis, defined by 30% SIC, is shown. Corresponding PCCs for the full physics
752 model (black), a simple melting model (red) and persistency (blue) in the ESS (right-lower panel of
753 the time evolution) are shown in the lower panel.

754 **Figure 12.** Trajectory of the two tankers over the ESS based on AIS data. The routes cross the ESS
755 from the Laptev Sea on 4 July 2014 to the port of Yamal on 31 July 2014, via the port of Pevek on
756 20 July 2014. The forward route is highlighted by green circles. The SIT (cm; colors) and SIC (%;
757 contours) averaged over the period of the forward route are shown.

758 **Figure 13.** Scatter plots of hourly vessel speeds (knots) and (a) daily mean SIT (cm) and (b) SIC
759 (%) in TOPAZ4 reanalysis from 4–30 July 2014. In each panel, the regression line of vessel speed
760 onto each variable is shown by broken line.

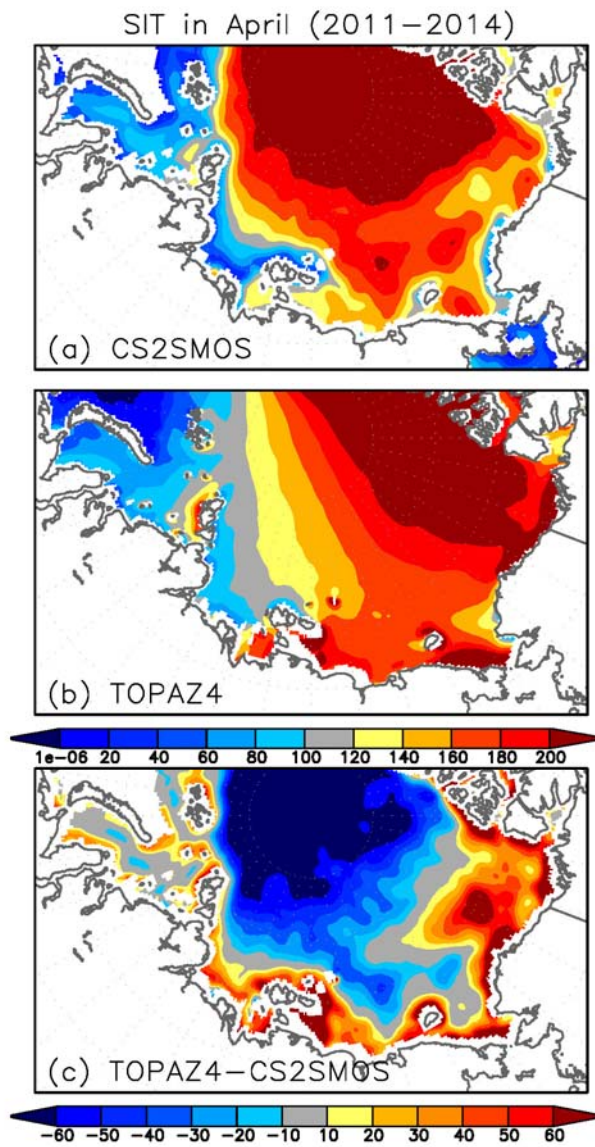
761



762

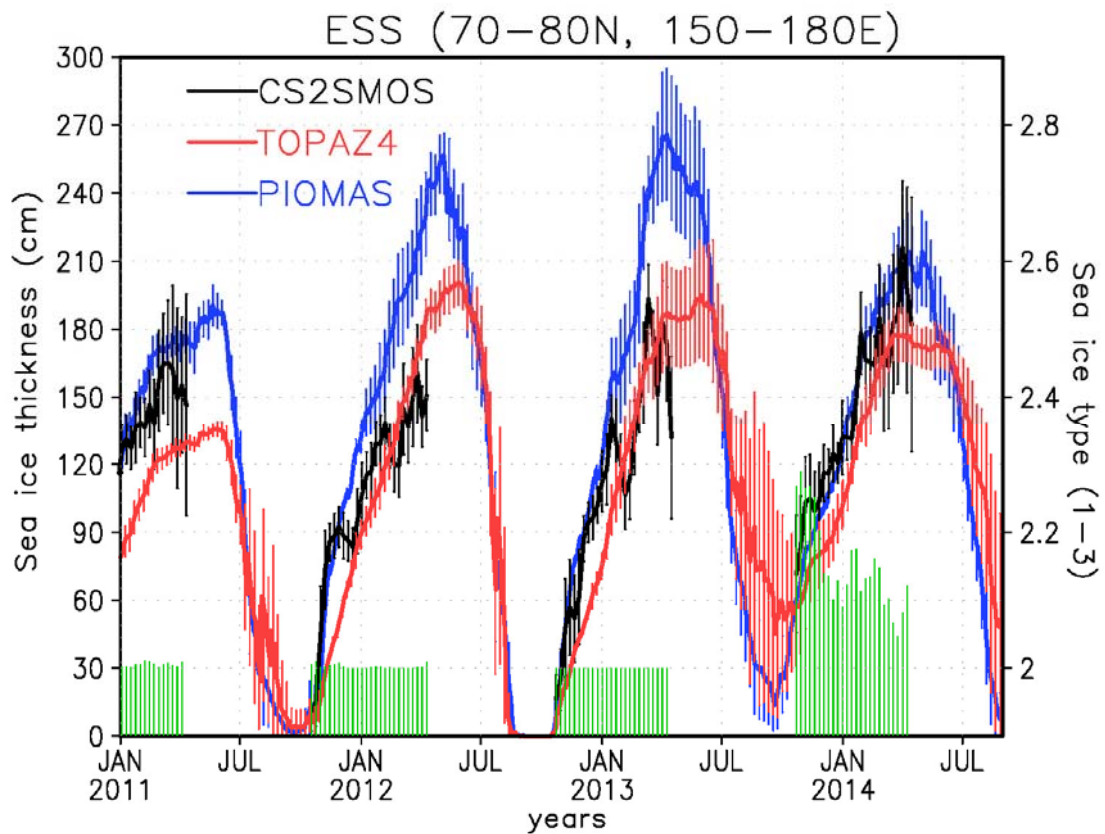
763 **Figure 1.** Spatial distribution of climatological monthly mean of SIT (cm) in July during 2011–
 764 2014: (a) PIOMAS, (b) TOPAZ4 reanalysis, and (c) their difference (cm). The boundaries of the
 765 ESS and Arctic marginal seas are indicated in panel a by thick and thin lines, respectively. In panel
 766 a, the trajectories of IMB buoys for 2011K, 2012I, 2012J, and 2014B (see Table 1 for the details of
 767 each buoy data) are shown by black, red, blue and green dots, respectively.

768



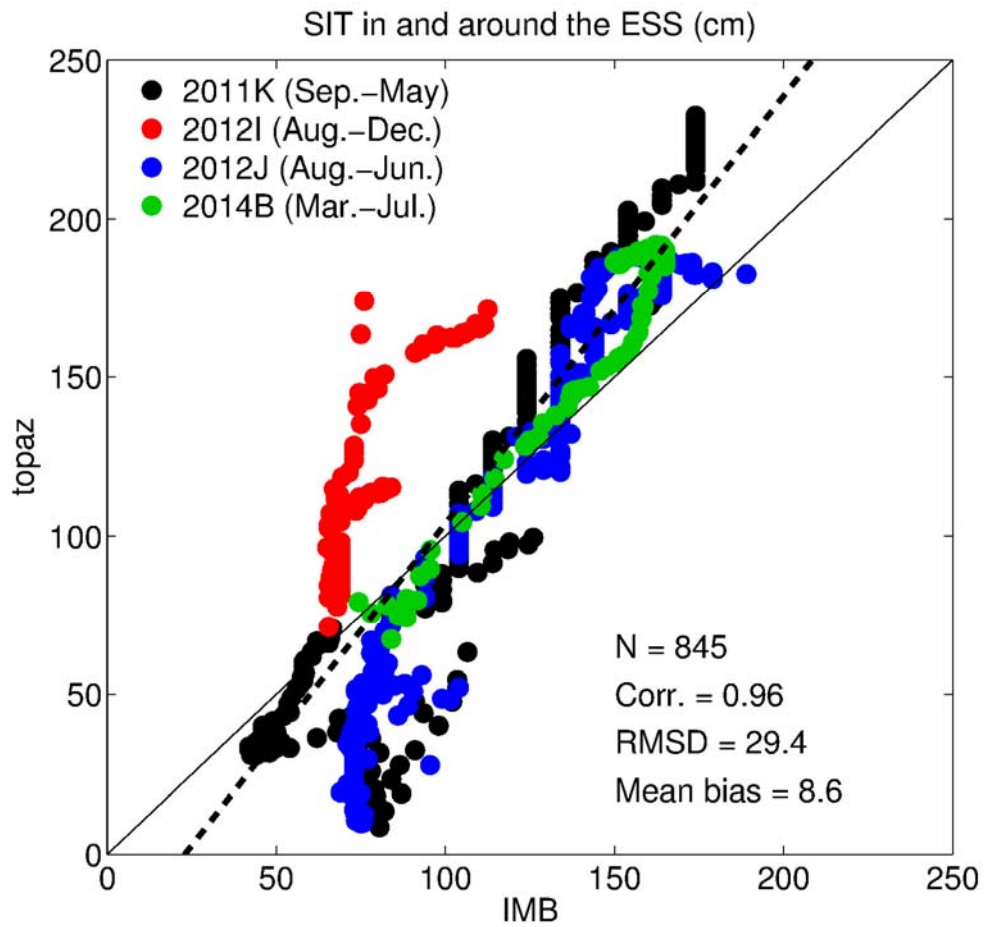
769

770 **Figure 2.** Spatial distribution of climatological monthly mean of SIT (cm) in April during 2011–
 771 2014: (top) CS2SMOS, (middle) TOPAZ4 reanalysis, and (bottom) their difference (cm).



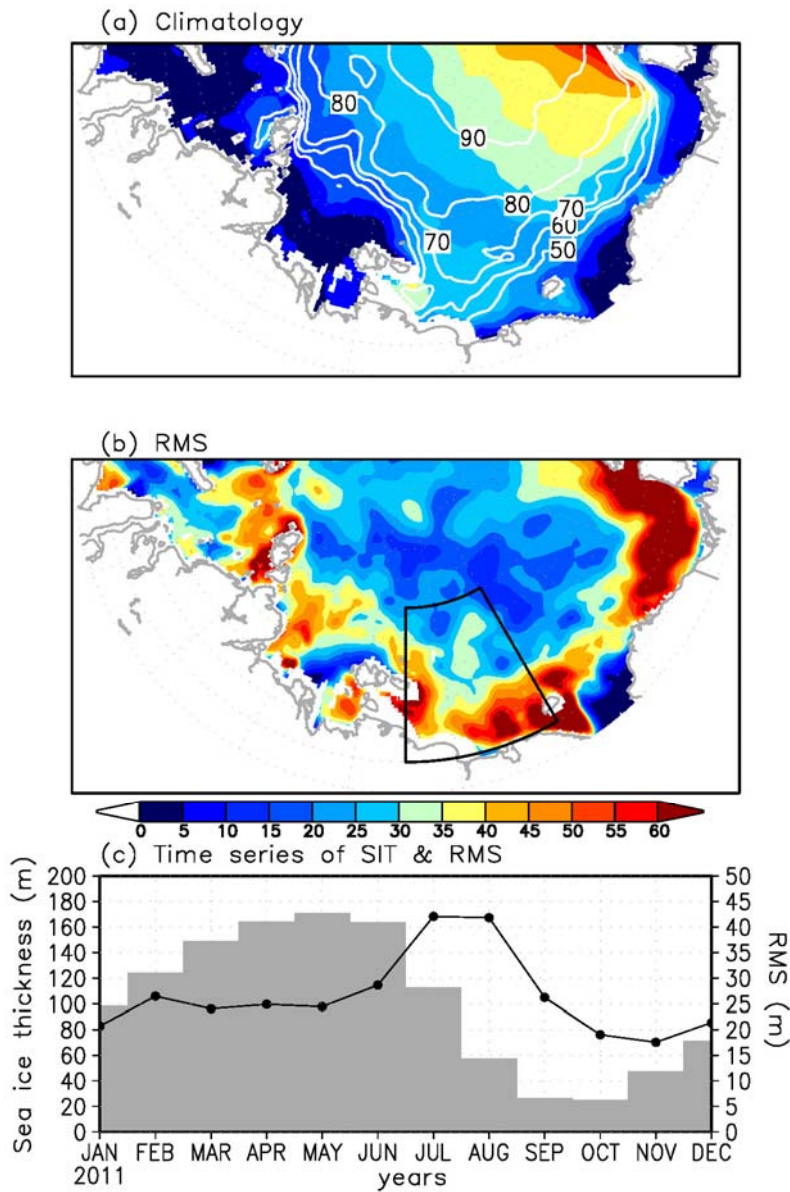
772

773 **Figure 3.** Time series of daily mean SIT (cm) averaged over the ESS (rectangular region denoted
 774 by black line in Fig. 1 (a)) derived from CS2SMOS (black), TOPAZ4 reanalysis (red), and
 775 PIOMAS (blue) from January 2011 to August 2014. For CS2SMOS data, 7 day mean values are
 776 shown. The standard deviations of area-averaged data are shown by vertical lines, respectively. The
 777 ice types (2: first-year ice, 3: multi-year ice) used for the choice of satellite SIT retrievals in
 778 CS2SMOS are shown by green bar. The scale for the ice type is located on the right vertical axis.



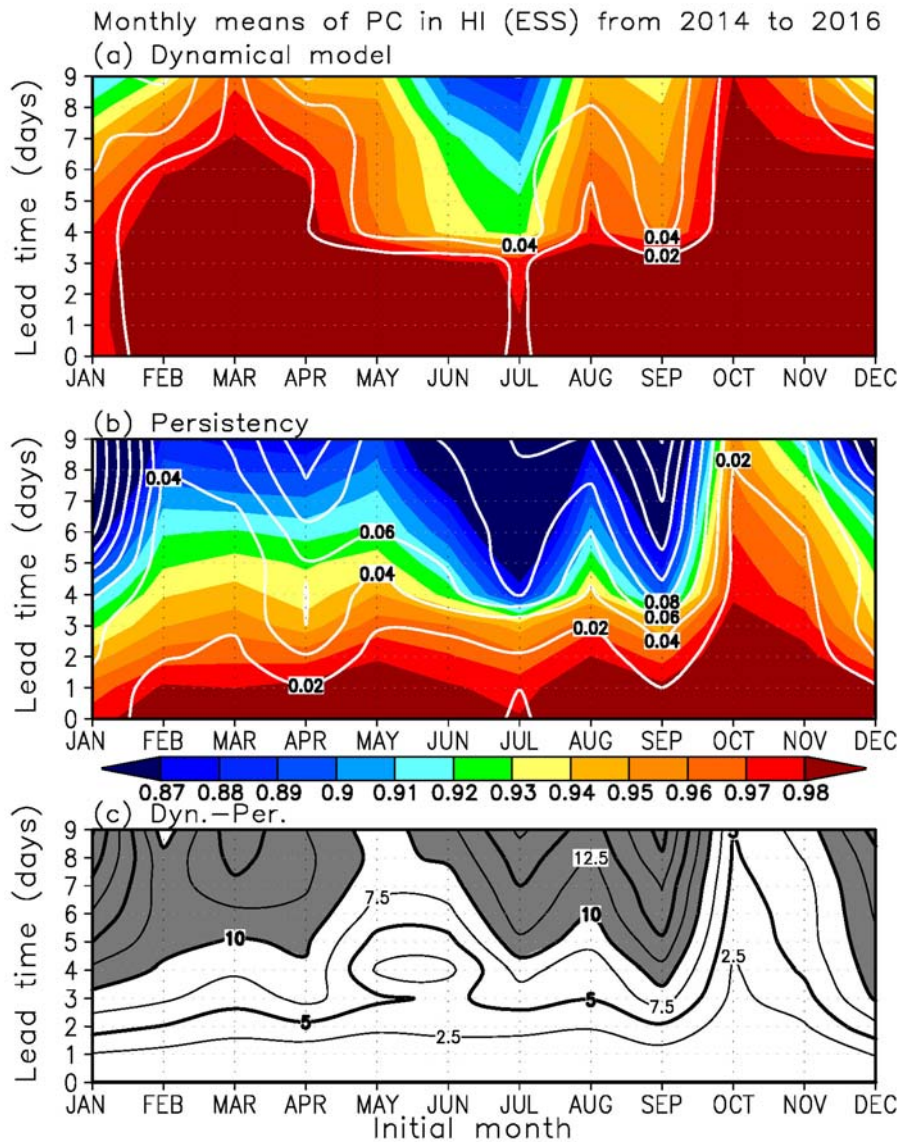
779

780 **Figure 4.** The comparisons of the daily mean SITs derived from IMB buoy data with the
 781 corresponding SIT in TOPAZ4 reanalysis data from 2011 to 2014 in and around the ESS. The SIT
 782 data are re-sampled per 7 days. The reference unit line and the regression lines onto IMB buoy data
 783 are shown by solid and dashed lines, respectively.



784

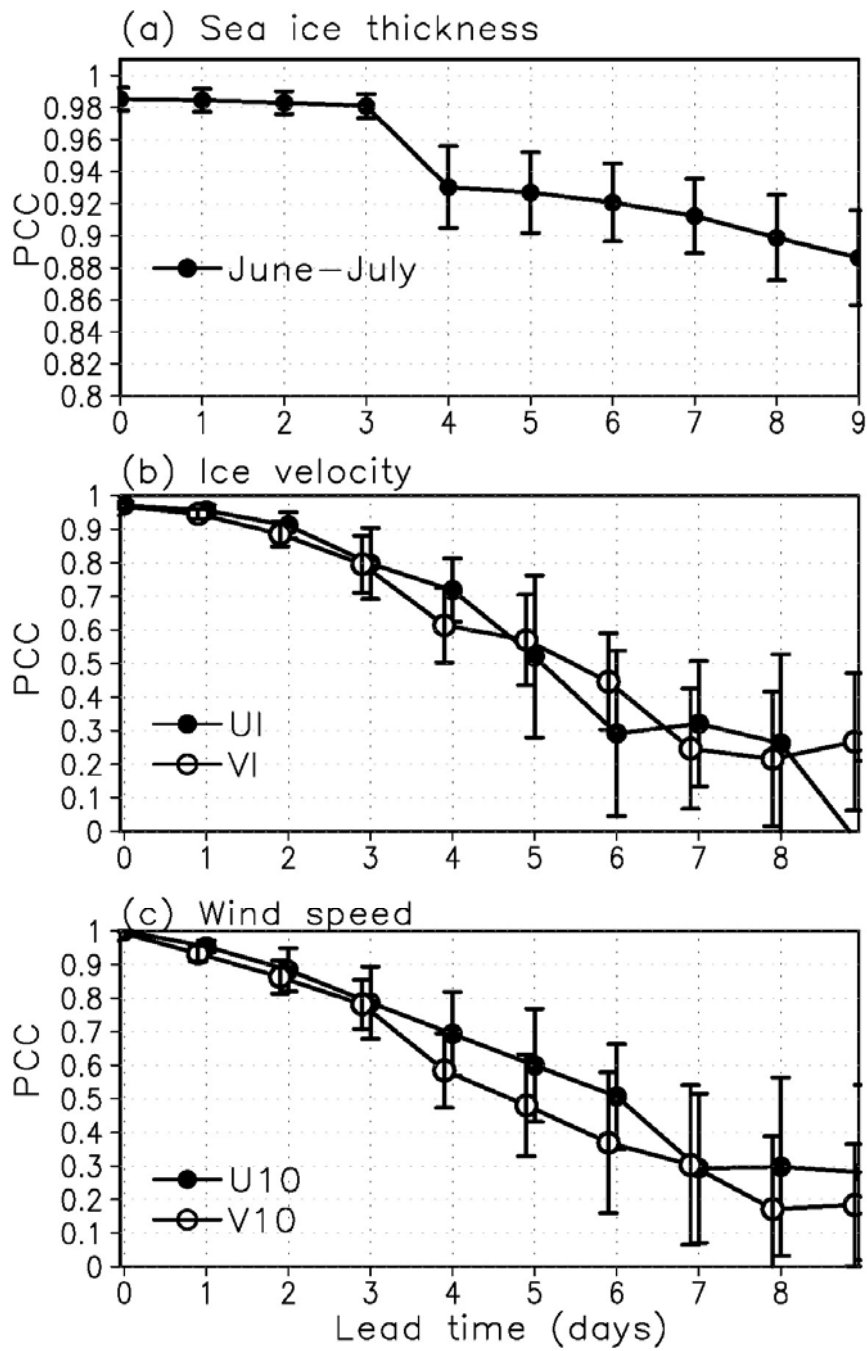
785 **Figure 5.** Spatial distribution of (a) monthly mean (colors) climatological SIT (m) in the TOPAZ4
 786 reanalysis and (b) the RMS variability of daily mean SIT (colors) in July during 2011–2014. The
 787 monthly mean of climatological SIC (white contours) in July is indicated in panel (a). The
 788 rectangular region enclosing the ESS (70°–80°N, 150°–180°E) is shown in panel (b). (c) Time
 789 series of monthly mean SIT (grey shade) and RMS of TOPAZ4 reanalysis (black line) averaged
 790 over the ESS. The scale of the RMS is indicated on the right axis.



791

792 **Figure 6.** The prediction skill (PCC) of SIT forecast in the ESS (70° – 80° N, 150° – 180° E) in each
 793 month obtained from (a) operational forecast model and (b) persistency of the initial value,
 794 averaged from 2014–2016. The standard deviations of the PCCs are shown with white contours. In
 795 panel c, the fraction of variance explained by operational forecast relative to the persistency (%) is
 796 shown by contour (the region where the fraction is larger than 10% is shaded).

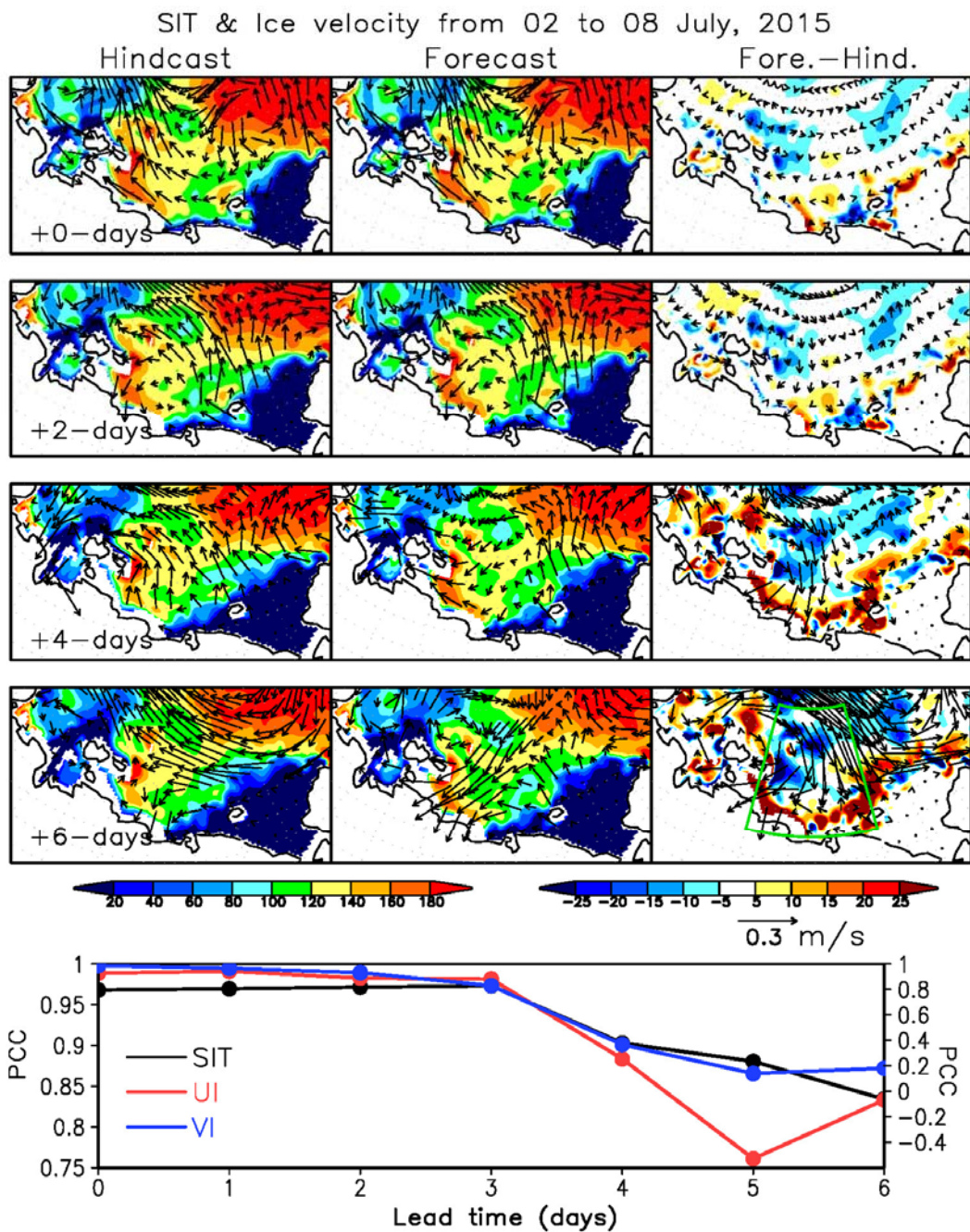
797



798

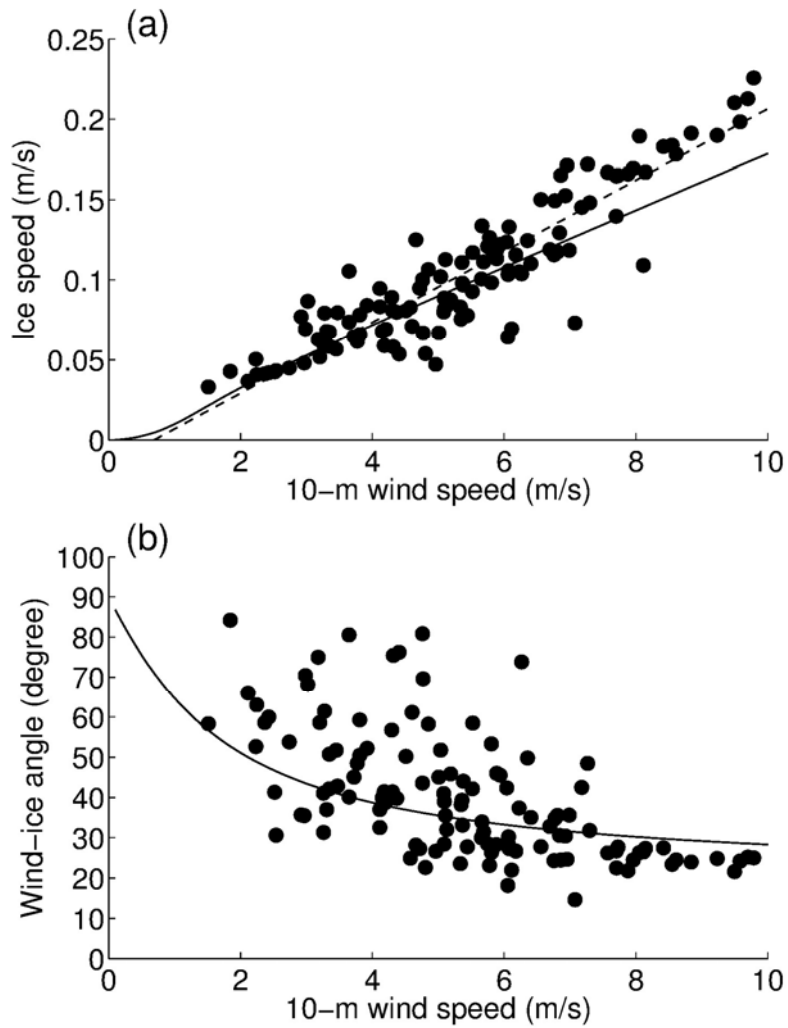
799 **Figure 7.** PCCs between forecast and analysis (a) SIT, (b) zonal and meridional ice speed, and (c)
 800 zonal and meridional surface wind speed from operational TOPAZ4 data in early summer
 801 (June–July) averaged on 2014–2016. Error bar indicates the standard deviation of the PCCs.

802



803

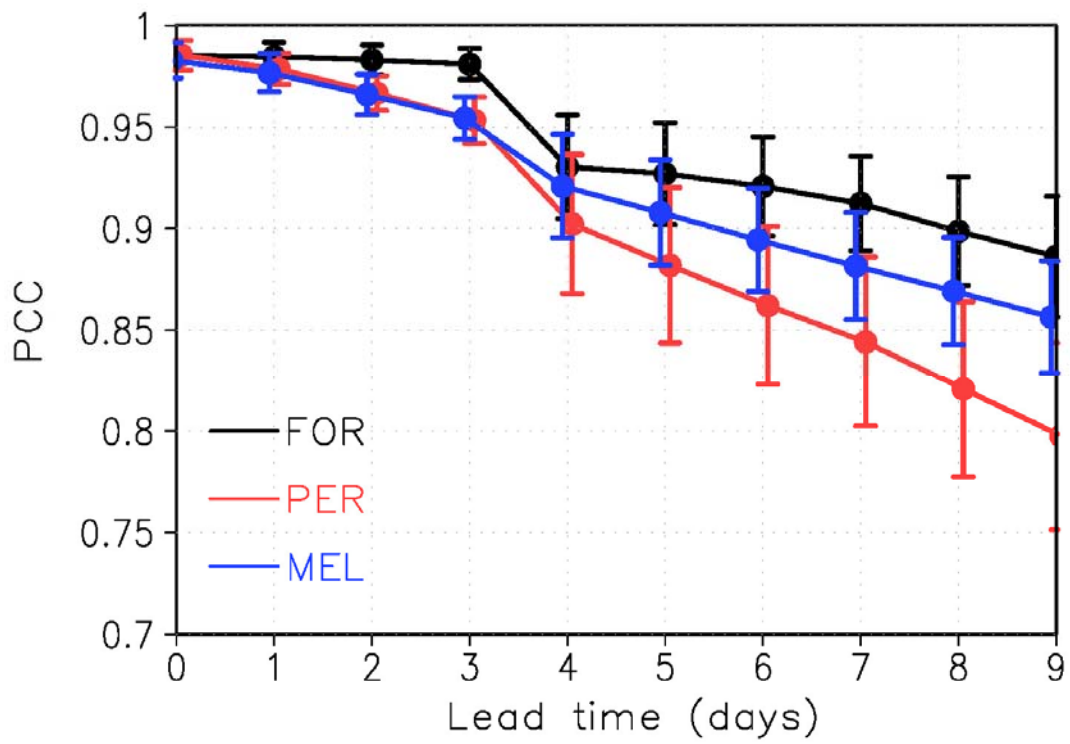
804 **Figure 8.** Temporal evolution of SIT (cm; colors) and ice velocity (m s^{-1} ; vectors) distribution for
 805 (left) analysis, (center) forecast, and (right) the difference between forecast and analysis at
 806 increasing lead times from +0 day to +6 days initialized on 2nd July 2015. The corresponding PCCs
 807 for the SIT (black), zonal (red) and meridional ice speeds (blue) in the ESS (right-lower panel of the
 808 time evolution) are shown in the lower panel. The scale for the PCCs of the zonal and meridional
 809 ice speeds is indicated on the right axis.



810

811 **Figure 9.** (a) Relationship between 10m wind speed (m s^{-1}) in the ERA Interim reanalysis data and
 812 sea ice speed (m s^{-1}) in the TOPAZ4 reanalysis averaged over a part of the ESS (72° – 76° N,
 813 150° – 170° E) during 1–31 July 2011–2014. Broken and solid lines indicate the regression line of
 814 ice speed on 10m wind speed ($y = 0.0224x - 0.0112$) and the theoretical ice speed estimated based
 815 on classical free-drift theory, respectively. (b) Angle (degrees) of sea ice velocity relative to surface
 816 wind vectors averaged over the ESS. Positive values indicate sea ice drift is to the right of the wind
 817 direction. Solid curve indicates the wind–ice velocity angle estimated based on classical free-drift
 818 theory.

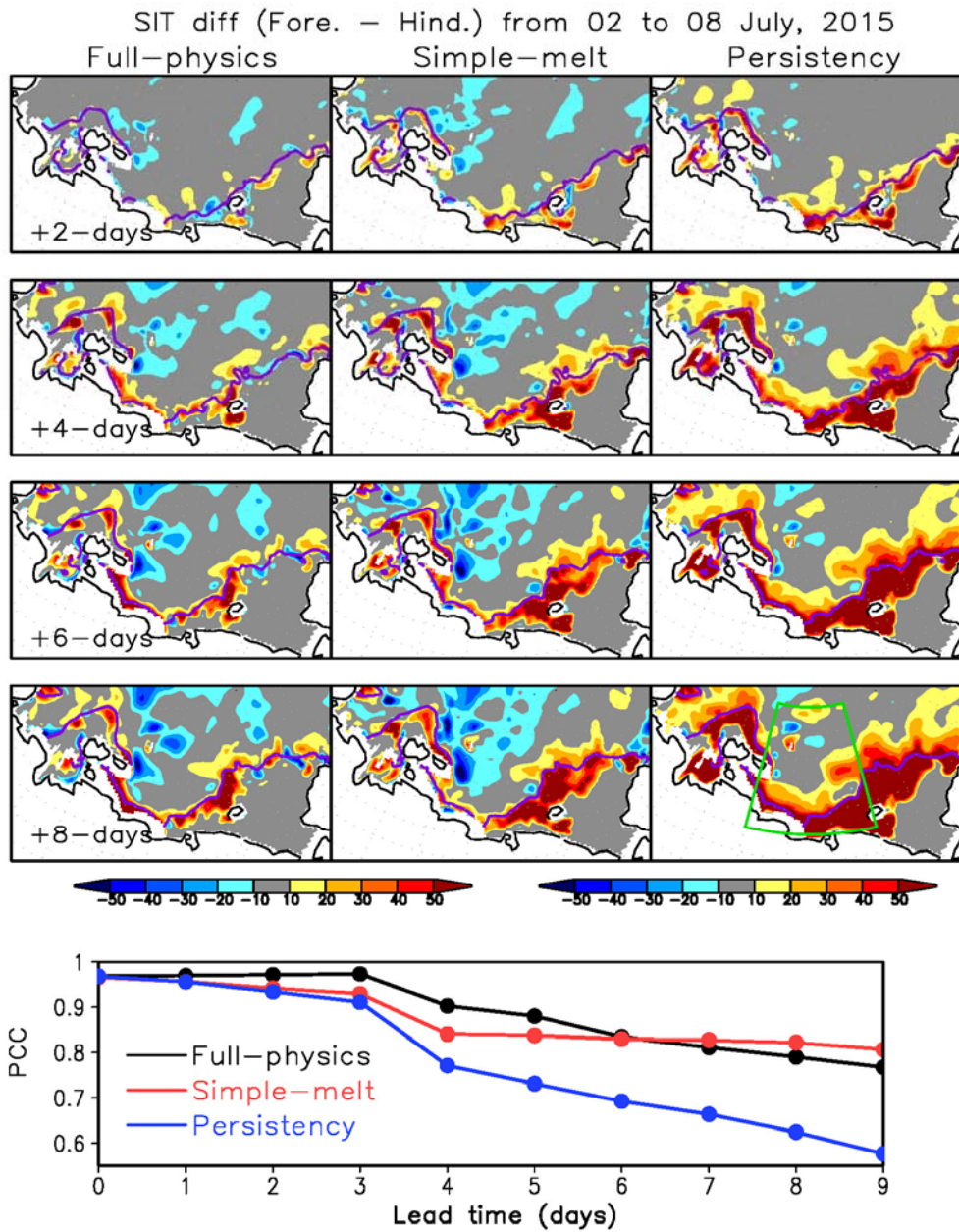
819



820

821 **Figure 10.** The PCCs between forecast and analysis SIT from the full physics model (black),
 822 persistency (red), and a simple melting model (blue) in early summer (June–July) averaged from
 823 2014–2016. Error bar indicates the standard deviation of the PCCs.

824

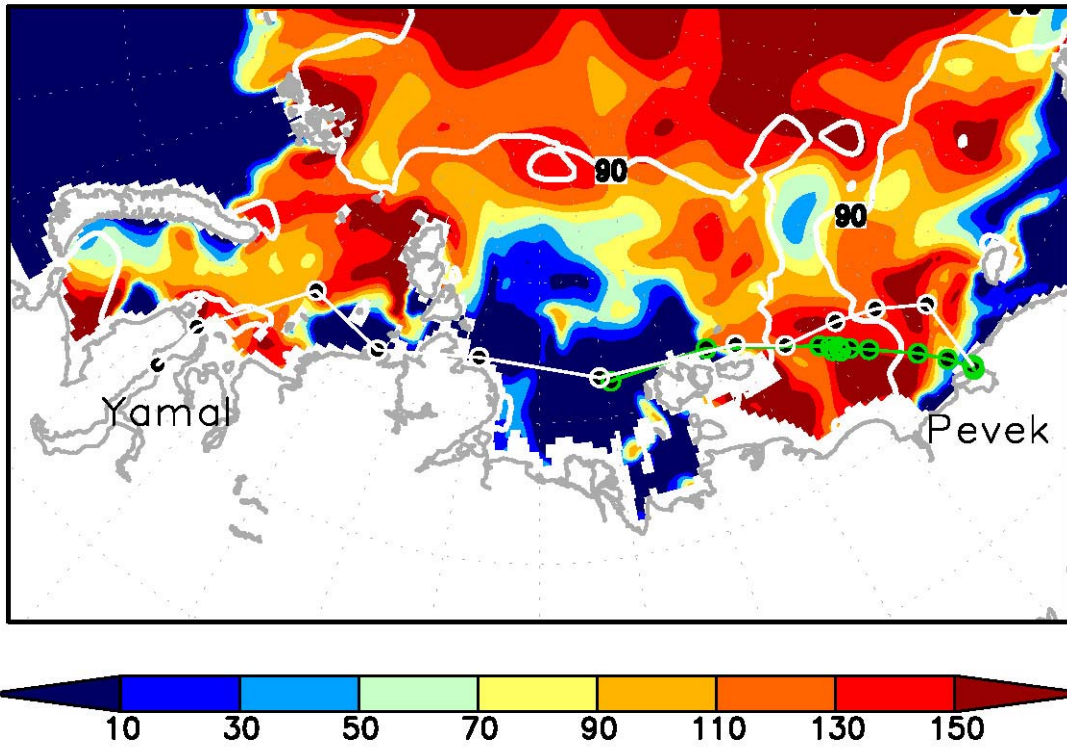


825

826 **Figure 11.** Temporal evolution of SIT differences (cm; colors) between the forecast and analysis
 827 data at lead times increasing from +2 to +8 days, initialized on 2nd July 2015. In each panel, the sea
 828 ice edge of the analysis, defined by 30% SIC, is shown. Corresponding PCCs for the full physics
 829 model (black), a simple melting model (red) and persistency (blue) in the ESS (right-lower panel of
 830 the time evolution) are shown in the lower panel.

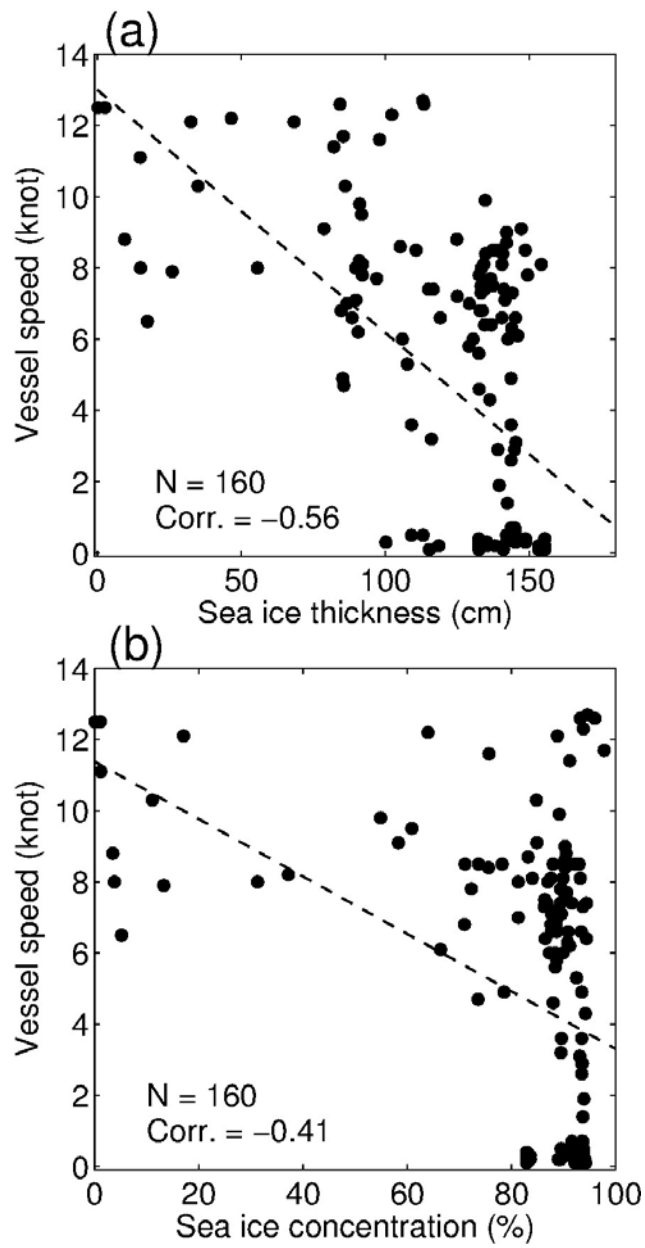
831

TOPAZ4-SIT & SIC in 04-15JUL2014



832

833 **Figure 12.** Trajectory of the two tankers over the ESS based on AIS data. The routes cross the ESS
834 from the Laptev Sea on 4 July 2014 to the port of Yamal on 31 July 2014, via the port of Pevek on
835 20 July 2014. The forward route is highlighted by green circles. The SIT (cm; colors) and SIC (%;
836 contours) averaged over the period of the forward route are shown.



837

838 **Figure 13.** Scatter plots of hourly vessel speeds (knots) and (a) daily mean SIT (cm) and (b) SIC
 839 (%) in TOPAZ4 reanalysis from 4–30 July 2014. In each panel, the regression line of vessel speed
 840 onto each variable is shown by broken line.